東京大学 大学院 新領域創成科学研究科 物質系専攻 修士論文

Oxygen vacancies in $SrTiO_3$ homoepitaxial films grown by pulsed laser deposition
(パルスレーザ堆積法で作製したチタン酸ストロンチウム薄膜中の酸素欠損)

指導教員： Harold Y. Hwang 印

学籍番号： 46140

氏名： 椋木 康滋

平成 18 年 1 月 31 日

Contents

1 Introduction **2**

1.1 Pulsed laser deposition (PLD) 2

1.2 Strontium titanate 9

1.3 Purpose of this thesis 14

2 Optics **18**

2.1 Introduction 18

2.2 Design 22

2.3 Installation and results 27

2.4 Summary 28

3 Homoepitaxial films of $SrTiO_3$ **31**

3.1 Introduction 31

3.2 Experiments 32

3.3 Results and discussion 33

3.3.1 Laser parameter effects 33

3.3.2 Growth temperature effects 38

3.3.3 Laser parameters and growth temperature 41

4 Conclusion **52**

5 Acknowledgements **54**

Chapter 1

Introduction

1.1 Pulsed laser deposition (PLD)

Pulsed laser deposition (PLD) is highly versatile and one of the most heavily used deposition techniques [1]. The pioneering works on PLD of high temperature superconductors were reported in 1987 and induced significant interest in studying the PLD process [2, 3]. Nowadays, PLD is known as one of the best deposition techniques to produce high-quality oxide thin films. Figure 1.1 shows the the schematic illustration of a PLD system. The principle of PLD involves rather complicated physical processes in spite of its ease of operation [4, 5]. A pulsed, intensive laser passes through an incident port of the chamber and is focused onto a surface of the target material inside the chamber. Immediately, significant ablation of the target material occurs in the form of a luminous plasma, the so-called "plume", in time scales of typically 10 nano-seconds. The plume then starts to expand into the surrounding ambient gas. The general features of the plume are their high ion and electron temperatures of the order of several thousand Kelvin, and their high degree of ionization. While expanding into the ambient gas, the plume decelerates due to collisions with gas atoms. Finally, the ablated materials are adsorbed on the heated substrate, where they might be thermally diffused across the surface and then re-evaporated once more to vacuum or become bonded as adatoms.

PLD is a suitable technique for the complex metal oxide growth [5]. Compared with other techniques like molecular beam epitaxy (MBE) or chemical vapor deposition (CVD), the advantages of PLD are the

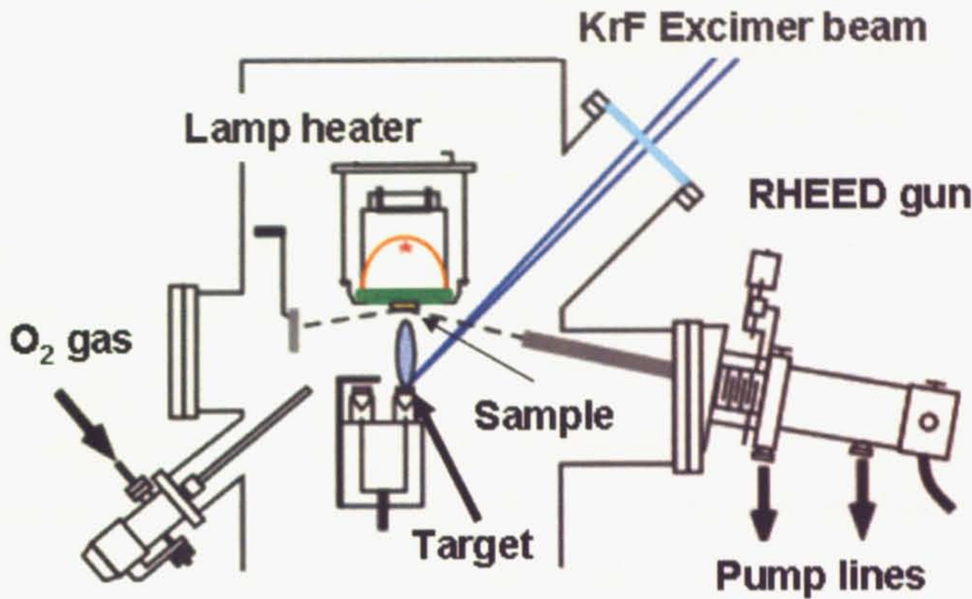

Figure 1.1: Schematic illustration of a PLD system.

following:

(1) Separation of the vacuum chamber and laser power source. This separation offers the flexibility of various geometrical configurations of the equipment. For example, the laser can be shared by more than one deposition chamber by arranging optics elements. Further, this decoupling allows reduction of the chamber dimensions and flexible combinations of the lasers and the ambient gas. There are many choices of the lasers for PLD growth, such as a pulsed CO_2 laser, a pulsed YAG laser, and a variety of excimer lasers (ArF, KrF, XeCl). The wide selection of the ambient gas is in principle available using the same apparatus.

(2) Availability for almost any condensed matter materials. The generation of very short laser pulses with a peak power exceeding 10^8 W/cm^2 has made it possible to ablate materials which have high melting temperatures.

(3) The almost ideal stoichiometric transformation of the target compounds to thin films. Above a threshold fluence which depends on target material, the laser removes several surface layers of the target completely. Thus, the deviation of the compound elements of the target and the films are negligibly small, which means the composition of the resultant films is expected to be the same as that of target material.

(4) The applicability of a wide pressure range of the ambient gases. One can use relatively high ambient gas pressure during deposition compared with other deposition techniques. Utilizing high ambient gas pressure makes it possible to fabricate compounds which are unstable at low pressure conditions.

(5) A highly kinetic method which often makes it possible to deposit high-quality thin films at lower temperatures because of the extra kinetic energy of the impinging particles. Sankur *et al.* reported that Ge heteroepitaxy was possible at 300 °C with PLD, while MBE required a substrate temperatures in excess of 700 °C [6].

On the other hand, the disadvantages of PLD are the following:

(1) Incorporation of impurities in the target. This is an unfavorable aspect of the stoichiometric transformation from a target to the films. The target of high purity is indispensable to fabricate the films of expected composition with high accuracy.

(2) The preferential ablation of the target materials. Dam *et al.* reported that the deviation of the [Sr]/[Ti] ratio for PLD grown homoepitaxial films of $SrTiO_3$ with lower fluence than 1.3 J/cm^2 [7]. Below the threshold fluence, such preferential ablation would result in off-stoichiometric deposition [8].

(3) The angular distribution of the plume. This angular distribution gives rise to the critical distribution of the thickness in the resultant films. It is known as a strong function of the target-substrate distance or laser spot dimensions. Due to this angular distribution, it is difficult to obtain uniform large area samples by PLD method. In addition, it is also reported that the energy of the particles in the plume has an angular distribution. Hansen *et al.* shows the angular distribution of laser ablated silver particles [9]. From their study, the highest energies occur in the perpendicular direction to the target surface and decrease as it deviates from that direction.

(4) Bombardment of the surface by highly energetic particles. In thermal deposition techniques such as MBE, the typical kinetic energy of the evaporated particles would be 0.1 eV, which is negligibly smaller than the bond strength of the surface atoms. On the other hand, in PLD growth, the kinetic energy of the impinging particles is the order of the bulk binding energy or larger in high vacuum conditions. It is well known that these highly energetic particles can displace surface and bulk atoms or create defects and vacancies. In addition, re-sputtering effects are repeated , as well as the deviation of the stoichiometry and implantation of impinging particles deeply into the substrate. For example, Sturm *et*

al. showed a reduction of Ag particle energy with increasing Ar pressure and a reduction of re-sputtering and interface mixing due to the scattering of dense assembly of Ag particles by Ar gases [10]. We always have to consider the possible effects on the qualities of the thin film caused by these advantages and disadvantages.

In PLD growth, the fundamental parameters are (1) the substrate temperature, (2) the ambient gas pressure in the chamber, (3) the target-substrate distance and (4) the deposition rate.

The substrate temperature is a dominant factor for the diffusion rate of the adatoms on the substrate surface. The diffusion rate of adatoms is often given by $D_S = D_0 \exp(-E_A/k_B T)$ where D_0 is pre-exponential factor, k_B is Boltzman constant and E_A is the activation energy for diffusion. Thermal diffusion is an indispensable process for adatoms to migrate to thermodynamically stable sites and minimize their surface energy. In general, higher growth temperature enhances the diffusion of adatoms and results in high quality epitaxial films. A simultaneous problem with enhancement of thermal diffusion by increasing the substrate temperature would be concomitant surface to bulk diffusion and bulk interdiffusion. This interdiffusion degrades the sharpness of heteroepitaxial interfaces and results in lower precision of layered structures. In PLD growth, the impinging particles from the target have kinetic energies which would also enhance the diffusion on the surface.

The presence of the ambient gases plays a critical role in the properties of the films in PLD growth. One of the remarkable effects is the collisions of the surrounding gas atoms with the impinging particles in the plume, which results in the reduction of the kinetic energies of particles and broaden their angular distribution. There are two different types of the ambient gas, inert gas and reactive gas. Ar gas is one of the most heavily used inert gases, and representative of the reactive gases would be oxygen gas. The oxide thin film deposition often takes place in a background oxygen gas in order to maintain a certain chemical equilibrium condition. This additional oxygen serves to compensate the oxygen vacancies in the resultant films, since the as-grown oxide films tend to be deficient in oxygen when deposition is performed in vacuum conditions. In addition, reactive scattering in oxygen ambient conditions can change the properties of the ionized particles in the plume via the formation of oxide molecules or clusters. Girault *et al.* reported the formation of YO molecular species from the ablation of $YBa_2Cu_3O_7$(YBCO) in oxygen ambient conditions [11]. Tachiki *et al.* reported that oxygen ambient gas degrades the plume

emission more quickly than the inert Ar gas ambient [12]. Oxygen reacts with the accelerated particles, consequently, reduces the electron temperatures and the amount of ionized and excited species in the plume.

When the film is deposited in relatively high ambient oxygen conditions ($\sim$ 100 mTorr), the target-substrate distance becomes a stringent parameter. For obtaining high quality YBCO films, there is an empirical scaling law between the oxygen partial pressure and the target-substrate distance [13, 14]. The origin of this scaling law is clearly related to the interaction of the plume and oxygen ambient gases. A qualitative explanation is the following: the kinetic energies of impinging particles in the plume would be extremely large near the target surface, and reduced as a function of the target-substrate distance due to the collisions with oxygen atoms. The highly excited particles could cause serious damage to the films if the substrate is placed close to the target. On the other hand, if the substrate is placed far away from a target, the deposition rate would be very low and the kinetic contribution to the surface diffusion of adatoms would not be available. Thus, there is an optimal condition where the moderately energetic atoms arrived on the substrate surface and result in producing high quality films due to kinetic assisted surface diffusion.

Figure 1.2 shows a comparison of PLD and other thermal deposition techniques with respect to the deposition rate and power flux as a function of energy of impinging particles. As seen, the average deposition rate of PLD is typically around 1 Å/sec with the frequency of 10 Hz. However, the instantaneous deposition rate during the ablation of plume would be 10^5 Å/sec, which is roughly two orders of magnitude higher than the other techniques. Such a high instantaneous particle flux is one of the characteristic features of PLD growth.

Above-mentioned parameters are in some sense "clean" parameters and intensive study has revealed several relationships between them. Compared with them, the effects of the laser parameters are less investigated and understood due to the tremendously complex mechanisms involved. In general, the mechanism of laser ablation is strongly affected by the laser wave length, the laser pulse duration (femto-second, pico-second, nano-second), laser fluence and target materials (metal, organic, solid).

For a certain material and a fixed laser wavelength, the laser fluence on the target surface plays a critical role in the properties of the plume. In the case of excimer laser, the laser-solid interaction

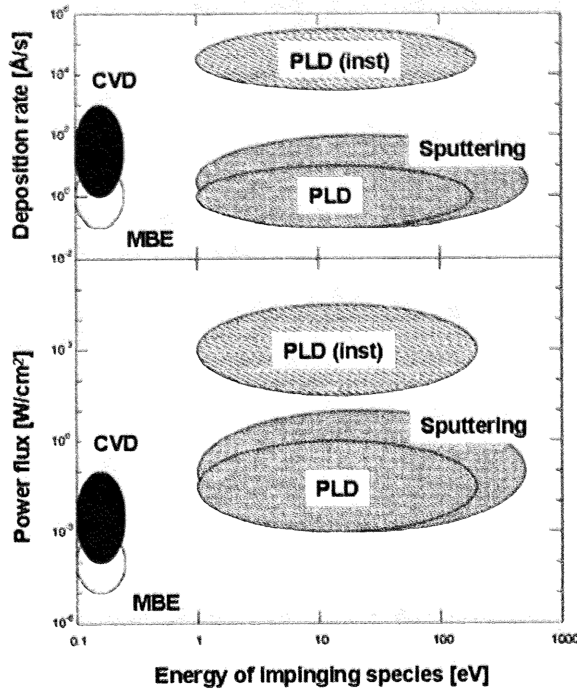

Figure 1.2: The deposition rate and the power flux as a function of the energy of the impinging particles for CVD, MBE, Sputtering and PLD (average and instantaneous). Adapted from Ref. [5].

is generally recognized as a thermal process: heating of the solid material, followed by melting and evaporation. In general, a thermal mechanism of laser ablation has shown the existence of a threshold fluence. As mentioned, below certain laser fluence, preferential ablation occurs and results in the non-stoichiometric transformation from a target to the films. Above the threshold fluence, stoichiometric deposition occurs and the kinetic energies of impinging particles increase rapidly.

The effect of the laser spot dimensions on the subsequent plume expansion has been examined in several studies. The modeling of gas dynamics has been efficiently used to explain the dynamics of expansion of the ablated plume into the vacuum. One of the successful examples of the gas dynamics modeling is explanation of the so-called "flip over effect" which means the smaller spot creates broaden angular distribution of the plume expansion. Thus, the film thickness profiles become sharper as the spot size are increased. This phenomenon was confirmed experimentally for $PbZrTiO_3$ (PZT) film deposition [15].

In order to control the film structure precisely, we placed emphasis on the layer-by-layer growth mode in which the growth of the following layer will not occur until the initial layer is fully formed. Reflection

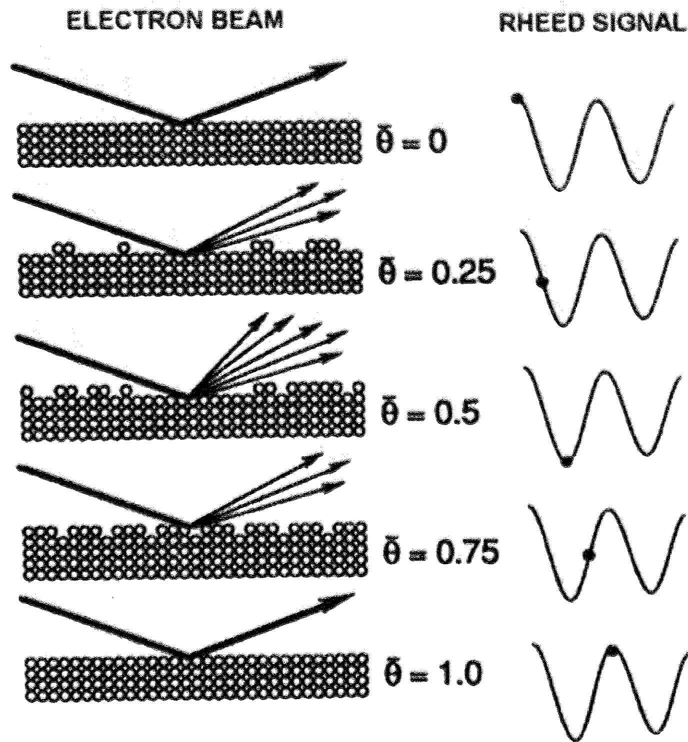

Figure 1.3: Schematic illustration of the principle of Reflection High-Energy Electron Diffraction (RHEED) intensity oscillation.

high-energy electron diffraction (RHEED) has been a powerful technique for *in-situ* monitoring of the film growth combined with MBE or PLD. Since the incident angle of electron beam is very small, the electrons interact with the topmost atoms of the surface, which makes RHEED very surface-sensitive. Figure 1.3 shows the principle of RHEED intensity, the periodic RHEED intensity oscillation corresponds to the periodic reconstruction of a smooth surface during deposition. By monitoring such oscillations accurately, we can control the structure of the film on an atomic scale.

1.2 Strontium titanate

Strontium titanate ($SrTiO_3$) is a typical perovskite-oxide compound as shown in Fig 1.4, in which the titanium atom is at the center and octahedrally surrounded by 6 oxygen atoms while strontium atoms are at the corners. At room temperature it is cubic with the lattice constant of 3.905 Å while it is tetragonal below 105 K [16]. In the stoichiometric form, it is a transparent insulator with the band gap of

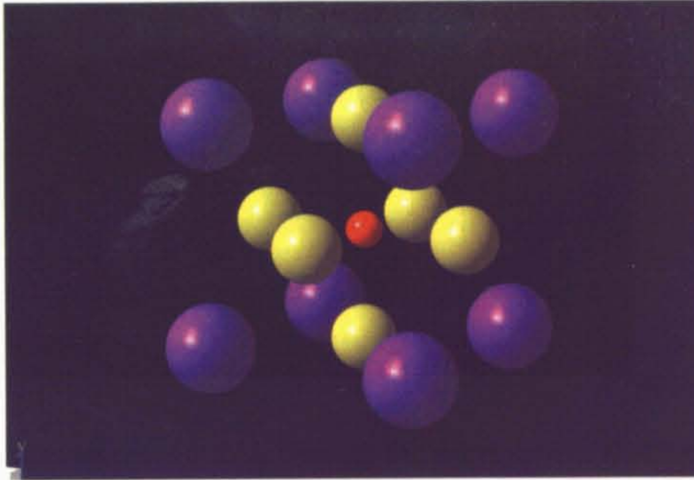

Figure 1.4: Atomic model of a unit cell of $SrTiO_3$. The red ball corresponds to titanium, the yellow balls to oxygen and the purple balls to strontium.

about 3.2 eV between the filled valance bands derived mainly from the oxygen $2p$ orbital and the empty conduction bands derived mainly from the titanium $3d$ orbital [17, 18, 19]. Substitutional doping of Nb on the Ti site, La on the Sr site or introduction of oxygen vacancies change the band-insulating $SrTiO_3$ to an electron-doped conductor. There has been a tremendous experimental effort to understand the electronic properties of n-type conducting $SrTiO_3$. The electrical transport properties of n-type $SrTiO_3$ were first investigated by Frederikse *et al*, who found degenerate semiconductor behavior with an electron effective mass much greater than the free-electron mass [20]. The dielectric constant of $SrTiO_3$ increases as the temperature decreases [21, 22, 23]. This large dielectric constant at low temperature strongly enhances the screening effect of the impurity potential and results in an extremely high electron mobility larger than 10,000 cm^2/Vs [24, 25]. $SrTiO_3$ becomes superconducting for the carrier density between about 1.0×10^{19} and 1.0×10^{20} cm^{-3} [26]. The superconducting transition temperature was found to be a function of the carrier density and reaches the maximum temperature of 0.3 - 0.4 K for a carrier density

of about 1×10^{20} cm^{-3} [27].

$SrTiO_3$ thin films have attracted much attention as a promising candidate for an alternative insulator for dynamic random access memory (DRAM) [28, 29, 30, 31]. In DRAM, the charge storage is determined by the capacitance $C = \epsilon_r \epsilon_0 A/d$, where ϵ_r is the relative dielectric constant, ϵ_0 is the permittivity of the free space, A is the area of the capacitor and d is the thickness of the dielectric layer. The conventional approach for increasing the storage density has been increasing C by decreasing d. However, the value of d has already been reduced to much smaller than 1 μm, where the dielectric properties start to be less reliable . Thus, many researchers are trying to incorporate large permittivity materials to DRAM. The dielectric constant of $SrTiO_3$ is as large as 300 at room temperature, much larger than that of conventional dielectric materials. However, the dielectric constants of $SrTiO_3$ thin films are usually lower than those of bulk, partly due to off-stoichiometry in films [32, 33].

Due to the availability of atomically flat (001) surface, $SrTiO_3$ has intensively been used as a substrate for epitaxial growth of perovskite oxides. In the (001) direction, $SrTiO_3$ consists of an alternating stack of SrO and TiO_2 atomic planes. Kawasaki *et al.* treated this surface with an NH_4F buffered HF solution with different pH values to selectively etch the SrO plane and obtained a uniform TiO_2-terminated surface [34]. Such a well-defined surface made it possible to realize atomic scale precision in epitaxial growth of perovskite oxides [35, 36]. In order to observe quantum effects in the electronic properties, electrons should be confined to shorter length than the de Broglie wavelength. Since the de Broglie wavelength is inversely proportional to the square root of the electron effective mass, and that of perovskite oxides is typically 100 times heavier than in conventional semiconductor like GaAs, the observation of quantum effects in perovskite oxides requires much smaller confinement than in semiconductor, namely, atomic scale modulations around $\sim$ 1 nm. This atomically flat surface accelerated the research of epitaxial perovskite oxides field for exploring novel quantum physical phenomena or creating oxide electronic devices.

Recently, Ohtomo *et al.* reported the relation between introduction of oxygen vacancies in $SrTiO_3$ homoepitaxial films and the characteristic growth dynamics of PLD [9]. They concluded that the properties of the homoepitaxial films and the growth mode are dominantly determined by interaction of the kinetics of surface crystallization and oxidation. The relaxation time of surface crystallization τ_{cryst} can

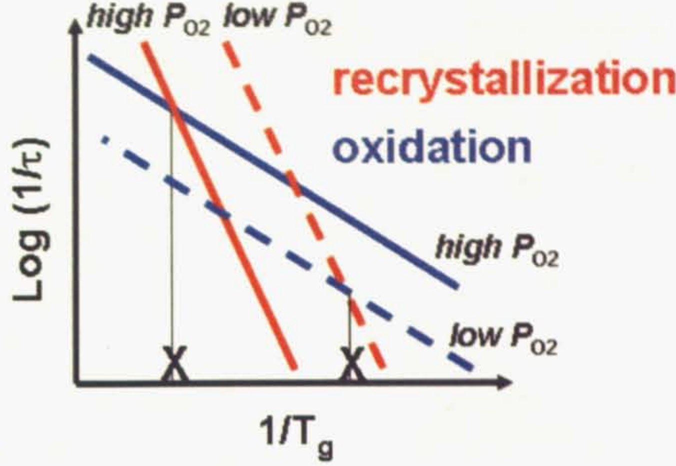

Figure 1.5: Schematic illustration of the interaction of the kinetics of surface crystallization and oxidation. The red lines shows the time constant of surface crystallization and the blue lines shows that of oxidation. The solid line is higher oxygen partial pressure condition and the dashed line is lower oxygen partial pressure condition.

be deduced from the RHEED intensity recovery after growth interruptions, and it is found to follow the Arrhenius form,

$$\tau_{\mathrm{cryst}}^{-1} = A \exp\left(\frac{-E_{\mathrm{cryst}}}{k_{\mathrm{B}} Tg}\right) \tag{1.1}$$

where A is a pre-exponential factor, E_{cryst} is the activation energy, k_{B} is the Boltzmann constant [38]. The relaxation time of the surface oxidation was measured by *in-situ* optical reflectivity measurements during PLD growth of monolayer $SrTiO_3$ and also found to be an Arrhenius form [11]. Figure 1.5 shows schematic illustration of interaction of the kinetics of surface crystallization and oxidation, in which the red lines indicate the time constant of surface crystallization and the blue lines indicate that of oxidation as a function of growth temperature. As growth temperature increases, thermal diffusion of adatoms is enhanced, resulting in a shorter τ_{cryst}. Both of these time constants are also a function of oxygen partial pressure as indicated by solid and dashed lines. When these time constants are matched, optimal layer-by-layer growth mode and a drastic metal-insulator transition were observed. Figure 1.6(A) shows contour lines of the number of unit cells of $SrTiO_3$ as functions of growth temperature and oxygen partial pressure at which the RHEED intensity oscillation became half of its initial amplitude. The optimal conditions of persistent layer-by-layer growth are indicated by $\times$. Figure 1.6(B) shows the room temperature carrier density as a function of growth temperature measured in six-probe Hall bar

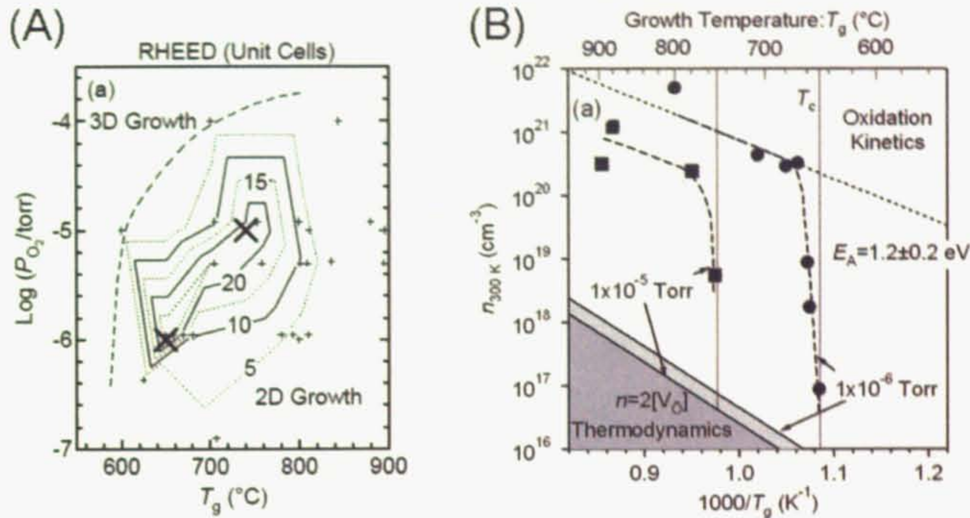

Figure 1.6: (A) Contour mapping of the number of unit cells at which the amplitude of RHEED intensity oscillations became half of its initial value as functions of growth temperature and oxygen partial pressure. The optimal conditions of persistent layer-by-layer growth mode are denoted by × for oxygen partial pressure at 1.0×10^{-5} Torr and 1.0×10^{-6} Torr. (B) The room temperature carrier density for the samples grown in 1.0×10^{-5} Torr and 1.0×10^{-6} Torr as a function of growth temperature. Adapted from Ref. [9].

geometries using evaporated Al Ohmic contacts. Above the optimal growth temperature of layer-by-layer growth mode, free carriers suddenly appear due to the implantation of oxygen vacancies in the $SrTiO_3$ films, which mean the formation of $SrTiO_3$ monolayer is formed before oxidation is completed.

Furthermore, Muller *et al.* reported the confinement of oxygen vacancies in PLD grown $SrTiO_3$ films with nanometer abruptness [40]. Figure 1.7(A) shows a low angle annular dark field (LAADF) STEM image of a homoepitaxial film of $SrTiO_3$ in which the oxygen deficient layer is visible as the bright layer. Spatial distribution of the Ti valence state is shown in Fig. 1.7(B) measured by electron energy-loss spectroscopy (EELS). The sudden appearance of Ti^{3+} signal indicates the localization of oxygen vacancies in finite area. They also show the ability to confine these vacancies down to three unit cell thicknesses, limited by vacancies clustering, which indicates the possibility of controlling of the electronic properties of $SrTiO_3$ the nanoscale precision [41].

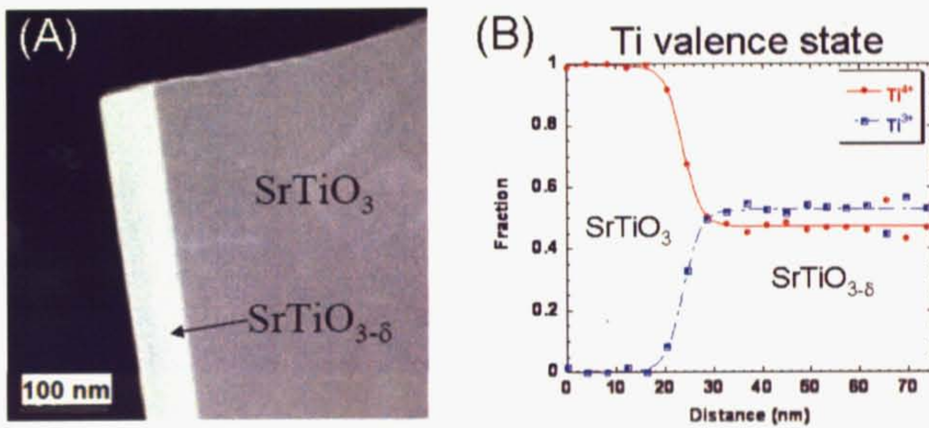

Figure 1.7: (A) A Low angle annular dark field (LAADF) STEM image of an oxygen deficient homoepitaxial $SrTiO_3$ film grown by PLD technique. Oxygen deficient layer is indicated as the bright layer which shows abrupt interface between stoichiometric substrate. (B) Spatial distribution of the signal of Ti valence state for an oxygen deficient homoepitaxial $SrTiO_3$ film. Adapted from Ref. [40].

1.3 Purpose of this thesis

As mentioned, the mechanism of PLD involves complex physical phenomena and is not well understood. Several parameters such as growth temperature, the oxygen partial pressure and target-substrate distance have been investigated since they are easily well controlled. In contrast, laser parameters are less investigated due to the difficulties of accurate control. The laser parameters are regarded as one of the main causes of instability and poor reproducibility of PLD. The purpose of this thesis is to study the effects of laser parameters to the properties of the resultant films. In order to control the laser parameters, we designed a zoom stage which allowed us to adjust laser spot size and fluence accurately. Homoepitaxial $SrTiO_3$ films were grown as a model growth system due to its simplicity. Besides laser parameters, we varied growth temperature simultaneously to further investigate its effect.

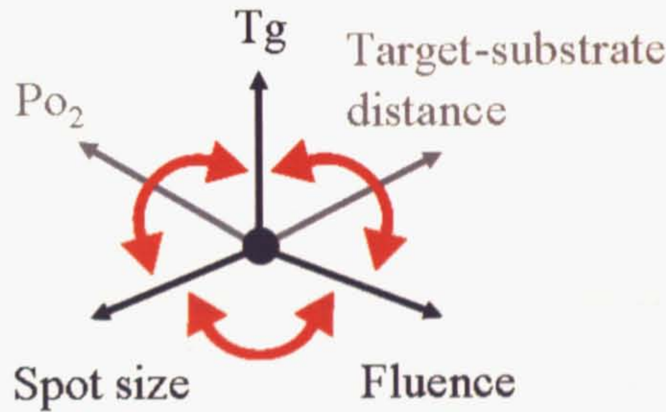

Figure 1.8: Schematic illustration of growth parameters. In this study, we varied growth temperature (Tg) and laser parameters such as spot size and fluence, while fixing the oxygen partial pressure (P_{O2}) and target-substrate distance.

Bibliography

[1] D. B. Chrisey and G. K. Hubler, *Pulsed Laser Deposition of Thin Films*, Wiley-Interscience, 1994.

[2] D. Dijkkamp, T. Venkatesan, X. D. Wu, S. A. Shaheen, N. Jisrawi, Y. H. Min-Lee, W. L. McLean and M. Croft, Appl. Phys. Lett. **51**, 619 (1987).

[3] X. D. Wu, D. Dijkkamp, S. B. Ogale, A. Inam, E. W. Chase, P. F. Miceli, C. C. Chang, J. M. Tarascon and T. Venkatesan, Appl. Phys. Lett. **51**, 861 (1987).

[4] P. R. Willmott and J. R. Huber, Rev. Mod. Phys. **72**, 315 (2000).

[5] P. R. Willmott, Prog. Surf. Sci. **76**, 163 (2004).

[6] H. Sankur, W. J. Gunning, J. DeNatale and J. F. Flintoff, J. Appl. Phys. **65**, 2475 (1989).

[7] B. Dam, J. H. Rector, J. Johansson, J. Huijbregtse and D. G. D. Groot, J. Appl. Phys. **83**, 3386 (1998).

[8] B. Dam, J. H. Rector, J. Johansson, S. Kars and R. Griessen, Appl. Surf. Sci. **96-98**, 679 (1996).

[9] T. N. Hansen, J. Schou and J. G. Lunney, Appl. Phys. Lett. **72**, 1829 (1998).

[10] K. Sturm, S. Fähler and H. U. Krebs, Appl. Surf. Sci. **154-155**, 462 (2000).

[11] C. Girault, D. Damiani, J. Aubreton and A. Catherinot, Appl. Phys. Lett. **55**, 182 (1989).

[12] M. Tachiki, M. Noda, K. Yamada and T. Kobayashi, J. Appl. Phys. **83**, 5351 (1998).

[13] H. S. Kim and H. S. Kwok, Appl. Phys. Lett. **61**, 2234 (1992).

[14] R. C. Rodríguez, D. R. Coronado, A. Iribarren, B. E. Watts, F. Leccabue and J. L. Peña, Appl. Phys. A **81**, 1503 (2005).

[15] M. Tyunina and S. Leppävuori, J. Appl. Phys. **87**, 8132 (2000).

[16] F. W. Lytle, J. Appl. Phys. **35**, 2212 (1964).

[17] A. H. Kahn and A. J. Leyendecker, Phys. Rev. **135**, A1321 (1964).

[18] K. C. Mishra, K. H. Johnson and P. C. Schmidt, J. Phys. Chem. Solids **54**, 237 (1993).

[19] M. I. Cohen and R. F. Blunt, Phys. Rev. **168**, 929 (1968).

[20] H. P. R. Frederikse, W. R. Thurber and W. R. Hosler, Phys. Rev. **134**, A442 (1964).

[21] H. E. Weaver, J. Phys. Chem. Solids. **11**, 274 (1959).

[22] R. C. Neville, B. Hoeneisen and C. A. Mead. J. Appl. Phys. **43**, 2124 (1972).

[23] T. Sakudo and H. Unoki, Phys. Rev. Lett. **26**, 851 (1971).

[24] O. N. Tufte and P. W. Chapman, Phys. Rev. **155**, 796 (1967).

[25] H. P. R. Frederikse and W. R. Hosler, Phys. Rev. **161**, 822 (1967).

[26] J. F. Schooley, W. R. Hosler and M. L. Cohen, Phys. Rev. Lett. **12**, 474 (1964).

[27] C. S. Koonce, M. L. Cohen, J. F. Schooley, W. R. Hosler and E. R. Pfeiffer, Phys. Rev. **163**, 380 (1967).

[28] T. Sakuma, S. Yamamichi, S. Matsubara, H. Yamaguchi and Y. Miyasaka, Appl. Phys. Lett. **57**, 2431 (1990).

[29] C. S. Hwang, S. O. Park, C. S. Kang, H. J. Cho, H. K. Kang, S. T. Ahn and M. Y. Lee, Jpn. J. Appl. Phys. **34**, 5178 (1995).

[30] G. M. Rao and S. B. Krupanidhi, J. Appl. Phys. **75**, 2604 (1994).

[31] S. B. Krupanidhi and G. M. Rao, Thin Solid Films **249**, 100 (1994).

[32] T. R. Taylor, P. J. Hansen, N. Pervez, B. Acikel, R. A. York and J. S. Speck, J. Appl. Phys. **94**, 3390 (2003).

[33] A. Tkach, P. M. Vilarinho, A. M. R. Senos and A. L. Kholkin, J. Euro. Cera. Soc. **25**, 2769 (2005).

[34] M. Kawasaki, K. Takahashi, T. Maeda, R. Tsuchiya, M. Shinohara, O. Ishiyama, T. Yonezawa, M. Yoshimotoi and H. Koinuma, Science **266**, 1540 (1994).

[35] M. Kawasaki, A. Ohtomo, T. Arakane, K. Takahashi, M. Yoshimoto and H. Koinuma, Appl. Surf. Sci. **107**, 102 (1996).

[36] G. Koster, B. L. Kropman, G. J. H. M. Rijnders, D. H. A. Blank and H. Rogalla, Appl. Phys. Lett. **73**, 2920 (1998).

[37] A. Ohtomo and H. Y. Hwang, unpublished.

[38] G. J. H. M. Rijnders, Ph. D. Thesis, Proefschrift Universiteit Twente, Enschede, 1999.

[39] X. D. Zhu, W. Si, X. X. Xi and Q Jiang, Appl. Phys. Lett. **78**, 460 (2001).

[40] D. A. Muller, N. Nakagawa, A. Ohtomo, J. L. Grazul and H. Y. Hwang, Nature **430**, 657 (2004).

[41] J. Mannhart and D. G. Schlom, Nature **430**, 620 (2004).

Chapter 2

Optics

2.1 Introduction

In order to investigate the effect of laser parameters, the first hurdle must be the systematic control of them with high accuracy and good repeatability. However, this is one of the main difficulties of PLD growth [1]. In general, the laser profiles are very sensitive to the voltage of discharge or the age of excimer gas. For example, the high voltage of discharge enhances not only the fluence but also divergence of the laser beam. Wagner *et al.* shows that a particular combination of the optical elements results in a laser spot with well-defined shape and homogeneous energy distribution [2]. This report is a great clue to address the control of the laser parameters indicating that the laser spot profiles depend very critically on the alignment of the optics elements.

As shown in Fig. 2.1, the PLD system consists of the separating vacuum chamber and laser power source, which gives us a degree of freedom to align the optical components between them.

Figure 2.2(A) shows a typical laser spot profile of the near focused image. The intensity profile is shown in Fig. 2.2(B) which is expressed as the form of sinc(x) for amplitude and as the form of $\text{sinc}^2(\text{x})$ for intensity. As seen, these function are continuously varying, and the distinct definition of spot size and fluence is extremely difficult.

Further, there are several limitations of this focusing mode due to its critical dependence on divergence of the incident laser beam. For example, the spot profile becomes larger at higher discharge voltage of

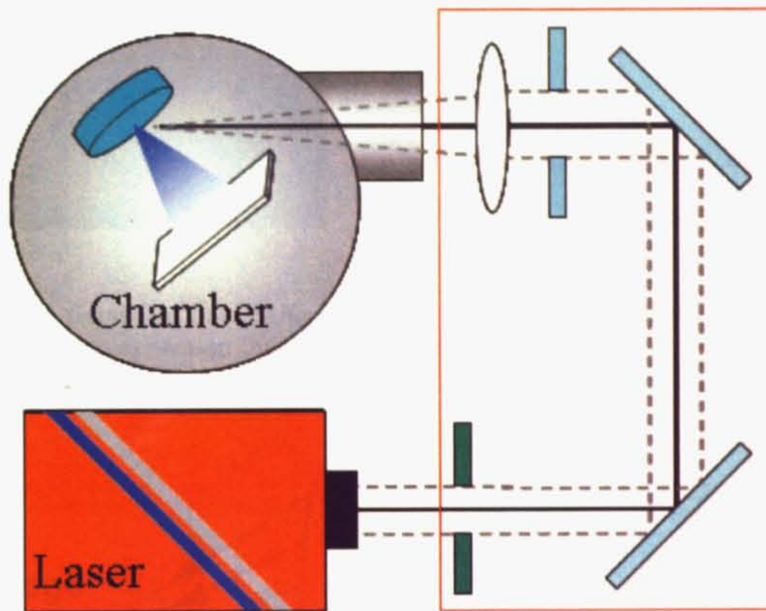

Figure 2.1: Schematic drawing of the PLD system.

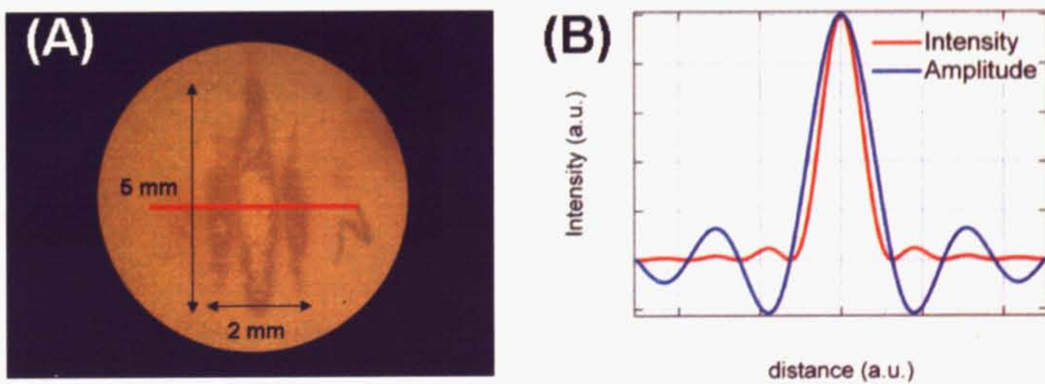

Figure 2.2: (A) The laser spot profile of the near focused image at the target position. (B) Theoretical profiles of intensity and amplitude at the cross section indicated by a red line in (A).

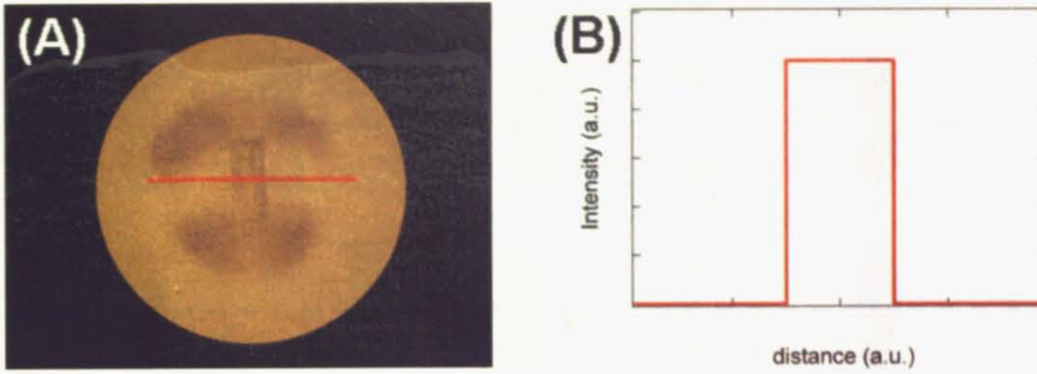

Figure 2.3: (A) The laser spot profile of the projection image at the target position. (B) Theoretical profiles of intensity at the cross section indicated by a red line in (A).

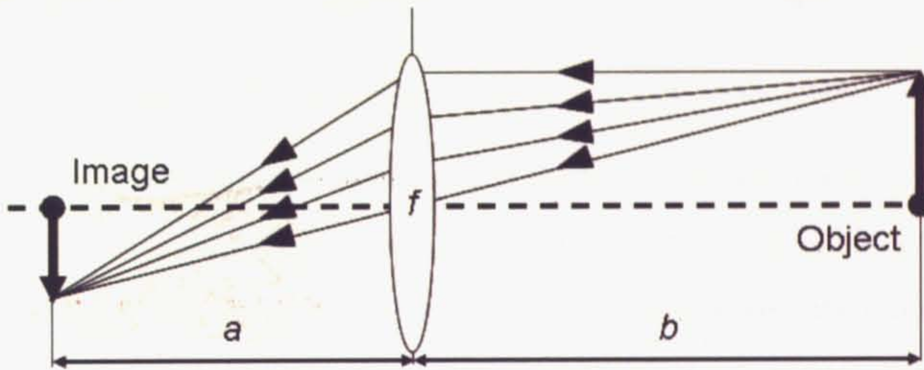

Figure 2.4: Schematic illustration of the formation of the imaging mode by an ideal thin lens element. All rays from an object point which pass through the lens are refracted to arrive at a certain image point.

the excimer laser, which makes it impossible to control the spot size and fluence independently. Another issue is the limitation of the focusing spot size. Assuming that the laser profile of KrF excimer laser which we used is a Gaussian beam, we can calculate the minimum size of the focused image given by

$$\omega_0 = f\theta \tag{2.1}$$

where w_0 is minimum beam waist, f is focal length and θ is divergence. Substituting the value 360 mm for f (which we used) and the standard divergence of the KrF excimer laser, 3×1 mrad, we obtained the minimum spot size of 0.36×1.08 mm^2. (Our actual divergence was significantly worse).

In contrast, Figure 2.3 shows a sharply defined image and homogeneous energy distribution. This is a projection of the aperture shape, so called "imaging mode". The imaging mode offers a well-defined

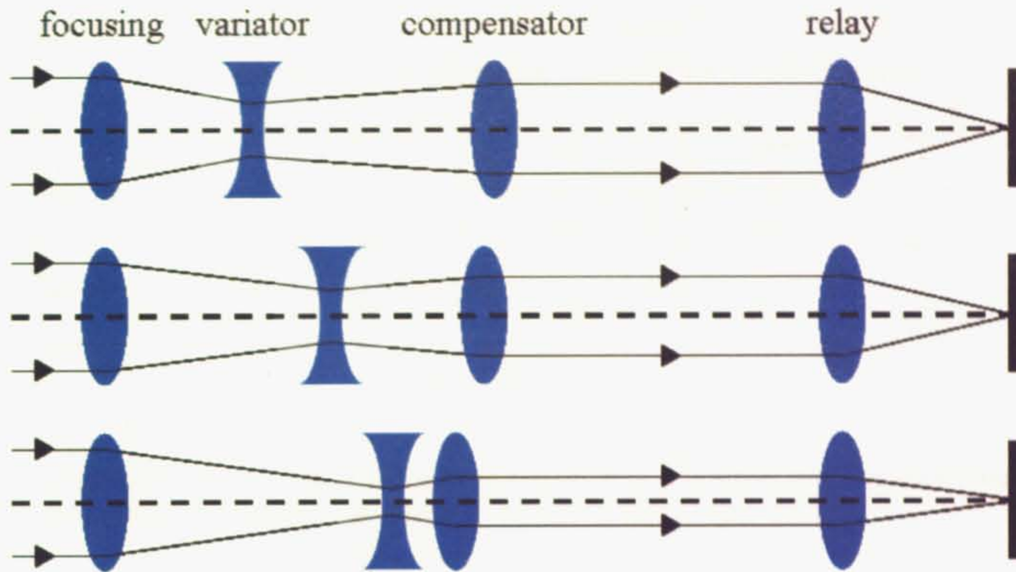

Figure 2.5: Movement of lens elements in a quartet-zoom stage.

spot shape, easy calculation of fluence and solution of the beam divergence together. The schematic illustration of an imaging formation is shown in Fig. 2.4. In order to realize image formation, the distance between an imaging screen and the lens denoted as a and between the lens and an object position denoted as b should satisfied the formula $1/a + 1/b = 1/f$. Under this condition, all rays emitted from a certain point of the object with different directions pass through the lens and are refracted to assemble at a certain point of the imaging screen. The resultant profile on the imaging screen is a projection of the object with the magnification of a/b. The imaging mode allows us to obtain well-defined sharp spot image with homogeneous energy distribution. However, there are several disadvantages of this imaging mode in our PLD system. The first issue is a requirement of longer distance b to obtain smaller magnification. As mentioned the magnification of the projection image is given by a/b, thus to create smaller magnification larger b is required. Since our laser has a serious divergence issue, the longer distance would lead to significant energy loss on the way to the lens. Another issue is a fixed magnification of the projection image. In order to obtain various magnifications, the distance a and b must be continuously and flexibly tuned. However our configuration of the target and laser is completely fixed, such a continuous adjustment is practically impossible. For example, we cannot adjust the length b shorter than 325 mm since it is the distance between an incident port and target surface.

In order to solve these issues, we utilized a principle of quartet-zoom stage. The schematic drawing

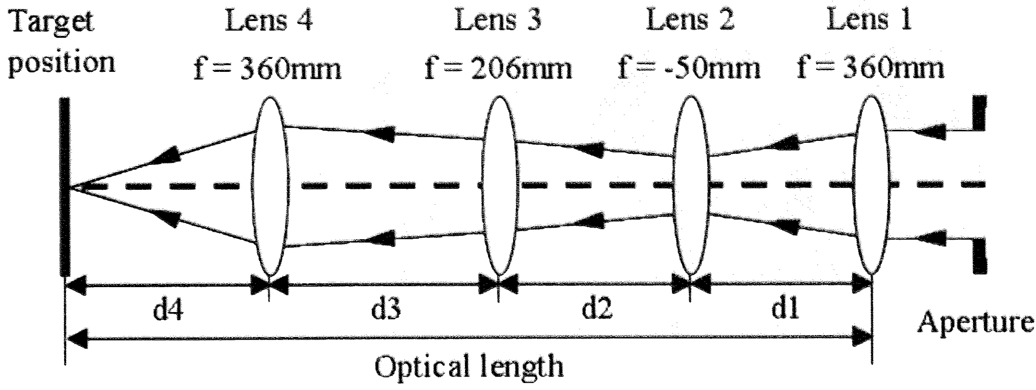

Figure 2.6: A schematic illustration of the optical system with 3 positive lens elements (Lens 1, Lens 3 and Lens 4) and a negative lens element (Lens 2) between Lens 1 and Lens 3.

of mechanism of a quartet-zoom stage is shown in Fig. 2.5. The 4 lens elements are slid along the optical path to project a virtual image of initial image with various magnifications. The individual lens elements are aligned, from the incident side, in order of a focusing lens, a variator lens, a compensator lens and a relay lens. The focusing lens concentrates the laser beam. The variator lens tunes the magnification and the compensator lens creates parallel or expanded beam. Thus, the first there lens elements act as a zoom system and tunes the magnification of the incident beam, resulting in the charge of the total magnification of the system. Since each individual lens element has a different role, the mechanical principle of a quartet-zoom system is relatively simple. The remarkable advantage is possibility of easy adjustment of the magnification with fixed total optical path.

Using a quartet-zoom stage, we designed a new optical system to control the laser parameters accurately. The schematic drawing of our optical system is shown in Fig. 2.6. By using this system, we have realized (1) homogeneous energy distribution, and (2) accurate adjustment of the laser spot size onto the target surface. In addition, we can produce a small virtual image of the large aperture, which enables us to obtain high fluence at the target surface.

2.2 Design

We designed the optical system by tracing the paths of the characteristic rays of light through the system. We used the matrix technique for numerical calculation [3]. Ray transfer matrix calculation

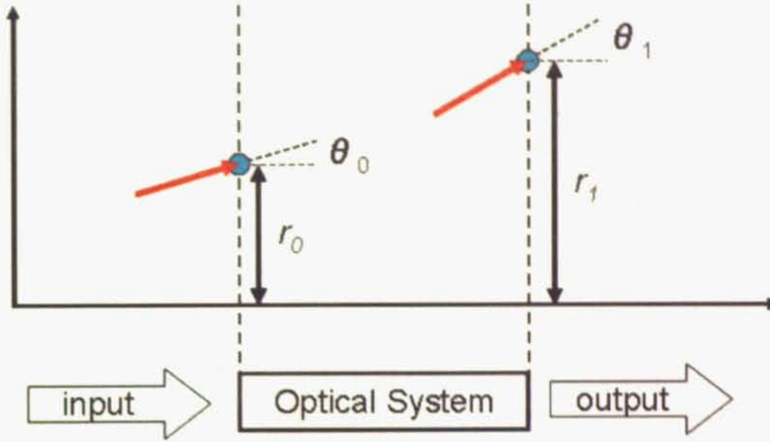

Figure 2.7: The schmatic drawing of the ray transfer matrix calculation. The input and output rays are described by a 2×1 column vector and the optical system by a 2×2 ray transfer matrix.

involves the construction of a ray transfer matrix which describes the optical system. Figure 2.7 shows a conception of this method. In this calculation, the rays are assumed to travel only within the single plane and described by a 2×1 column vector, whose elements represent the height r from the center and the oblique angle θ with respect to the optical axis.

$$\boldsymbol{r} = \begin{pmatrix} \theta \\ r \end{pmatrix} \tag{2.2}$$

The optical system is described by a 2×2 ray transfer matrix which relates a ray matrix at the output to its input. Here I introduced two types of ray transfer matrices, a transfer matrix and a refraction matrix. A transfer matrix describes translation by distance d and given by

$$\boldsymbol{T} = \begin{pmatrix} 1 & 0 \\ d & 1 \end{pmatrix} \tag{2.3}$$

The ray after the path of d is described by

$$\boldsymbol{T} \times \boldsymbol{r} = \begin{pmatrix} 1 & 0 \\ d & 1 \end{pmatrix} \times \begin{pmatrix} \theta \\ r \end{pmatrix} = \begin{pmatrix} \theta \\ d\theta + r \end{pmatrix} \tag{2.4}$$

A refraction matrix describes the refraction of a ray by a single thin lens element and is given by

$$\boldsymbol{R} = \begin{pmatrix} 1 & -\frac{1}{f} \\ 0 & 1 \end{pmatrix} \tag{2.5}$$

where f is a focal length of the individual lens element. We can obtain the ray matrix at the output plane of a lens element as

$$\boldsymbol{R} \times \boldsymbol{r} = \begin{pmatrix} 1 & -\frac{1}{f} \\ 0 & 1 \end{pmatrix} \times \begin{pmatrix} \theta \\ r \end{pmatrix} = \begin{pmatrix} \theta - \frac{r}{f} \\ r \end{pmatrix} \tag{2.6}$$

In order to describe a cascade of optical components, a ray transfer matrices may be multiplied together in appropriate order to obtain the system matrix for the compound optical system.

As shown in Fig. 2.6, our optical system consists of 1 aperture and 4 individual lens elements. Thus, we introduced the 4 refraction matrices and the 4 transfer matrices.

$$\boldsymbol{R}_1 = \begin{pmatrix} 1 & -\frac{1}{360} \\ 0 & 1 \end{pmatrix} \tag{2.7}$$

$$\boldsymbol{R}_2 = \begin{pmatrix} 1 & \frac{1}{50} \\ 0 & 1 \end{pmatrix} \tag{2.8}$$

$$\boldsymbol{R}_3 = \begin{pmatrix} 1 & -\frac{1}{206} \\ 0 & 1 \end{pmatrix} \tag{2.9}$$

$$\boldsymbol{R}_4 = \begin{pmatrix} 1 & -\frac{1}{360} \\ 0 & 1 \end{pmatrix} \tag{2.10}$$

$$\boldsymbol{T}_1 = \begin{pmatrix} 1 & 0 \\ d1 & 1 \end{pmatrix} \tag{2.11}$$

$$\boldsymbol{T}_2 = \begin{pmatrix} 1 & 0 \\ d2 & 1 \end{pmatrix} \tag{2.12}$$

$$T_3 = \begin{pmatrix} 1 & 0 \\ d3 & 1 \end{pmatrix} \quad (2.13)$$

$$T_4 = \begin{pmatrix} 1 & 0 \\ d4 & 1 \end{pmatrix} \quad (2.14)$$

By multiplying these matrices, we could obtain the system matrix $\boldsymbol{A}$ as follows:

$$\boldsymbol{A} = \begin{pmatrix} A & B \\ C & D \end{pmatrix} = \boldsymbol{T}_4 * \boldsymbol{R}_4 * \boldsymbol{T}_3 * \boldsymbol{R}_3 * \boldsymbol{T}_2 * \boldsymbol{R}_2 * \boldsymbol{T}_1 * \boldsymbol{R}_1 \quad (2.15)$$

where we have 4 variables, $d1$, $d2$, $d3$ and $d4$. For further calculation, we introduced another variable "Optical Length" ($OL = d1 + d2 + d3 + d4$). Here we use OL as an independent parameter instead of $d3$. There is a limit to the value for OL due to the geometrical relation of the vacuum chamber and the laser. We used several values such as 2500, 3000, 3500 and 4000. Using the system matrix $\boldsymbol{A}$, we can obtain the ray matrix at the target position;

$$\boldsymbol{A} \times \boldsymbol{r} = \begin{pmatrix} A & B \\ C & D \end{pmatrix} \times \begin{pmatrix} \theta \\ r \end{pmatrix} = \begin{pmatrix} A\theta + Br \\ C\theta + Dr \end{pmatrix} \quad (2.16)$$

As shown in Fig. 2.4, the condition for creating a virtual image on the target point is gathering the ray which depart from the one point of an object with various oblique angle to one point on an image position. To eliminate the oblique angle dependence, the required condition is that C, the lower left element of the system matrix $\boldsymbol{A}$, must be equal to zero. Therefore we can further reduce the number of independent parameters. Here we express $d4$ as a function of $d1$ and $d2$. The magnification of a virtual image M is given by the lower-right element of the $\boldsymbol{A}$, namely D which can be expressed as functions of $d1$ and $d2$. We also calculated the magnification of Lens 4 in order to confirm whether of the laser is within the diameter of Lens 4. We obtained the magnification of the virtual image at the target position and at Lens 4, M_T and M_L, respectively, as functions of $d1$ and $d2$ as shown in Figure 2.8.

From Fig. 2.8, we found that $d1$ must be long while $d2$ must be short to realize smaller magnification

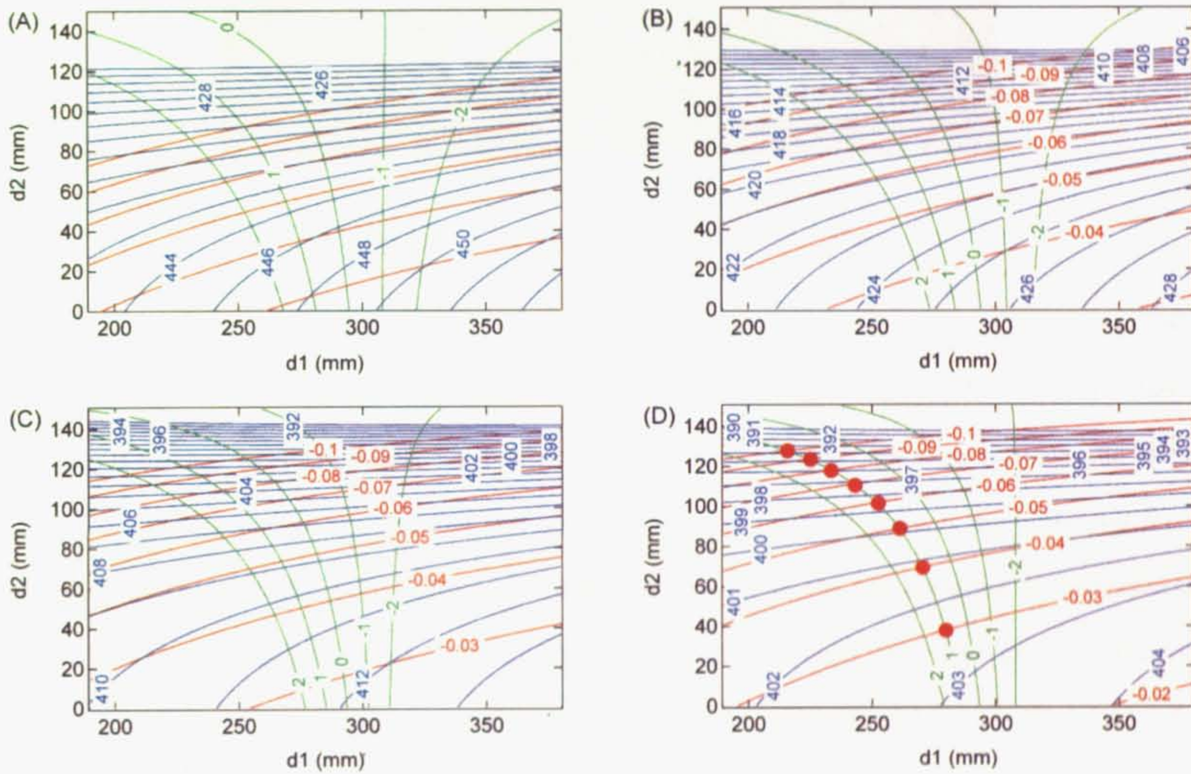

Figure 2.8: Contour map of the calculated magnification at the target position (red lines) and at Lens 4 (green lines) and distance *d4* (blue lines) as functions of d1 and d2 for the case of OL=2500 mm (A), 3000 mm (B), 3500 mm (C) and 4000 mm (D). The red circles indicate the values of *d1* and *d2* which were used in our experiment.

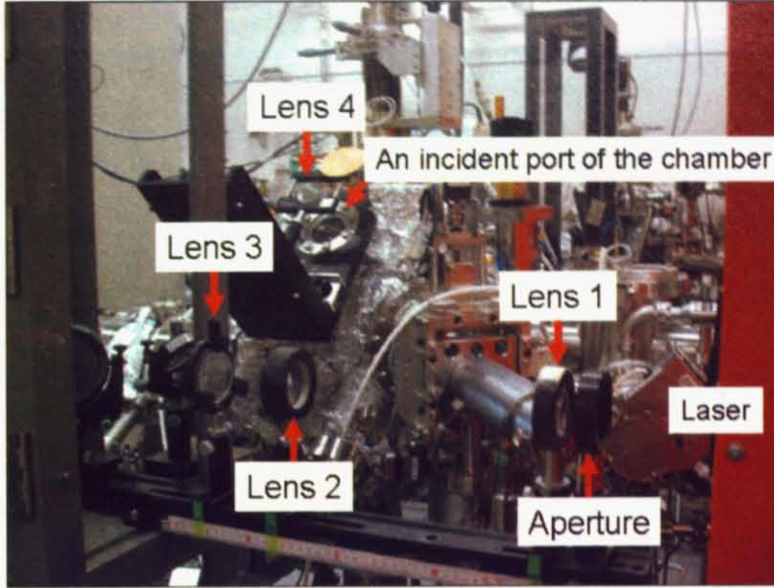

Figure 2.9: A photograph of the optical system.

(reduced image). Due to the design of the vacuum chamber the minimum value of $d4$ is 325 mm, which is the distance between the incident port of the chamber and the target surface. We confirmed that this condition is fulfilled in all the cases. For realizing further ideal situation, we want to make the distance between an incident port of the chamber and Lens 4 as short as possible. Namely, we prefer less focused laser passing through the port in order to avoid serious damage to the silica window by intensive laser power. The shorter distance of $d4$ is realized in the case of the longer OL. The green contour lines denote M_L calculated on the assumption that the incident laser is the parallel beam. Those lines of M_L = 0 means the laser beam would be focused on Lens 4. Thus, we selected the lines $M_L = 1$ to avoid forming focused points along the system, which will destroy the optical components. Considering the above results, we set OL to be 4000 mm and tuned $d1$ and $d2$ as indicated by red dots in Fig. 2.8(D).

2.3 Installation and results

Based on the above calculation, we installed the optical system between the laser and the chamber as shown in Fig. 2.9. Subsequently, we took the profiles of the laser spot images on the target surface as shown in Fig. 2.10. It should be emphasized again that these distinct square images aligned in a circle are the virtual images of the original aperture (5×15 mm^2). Table 2.1 summarizes the actual size and the

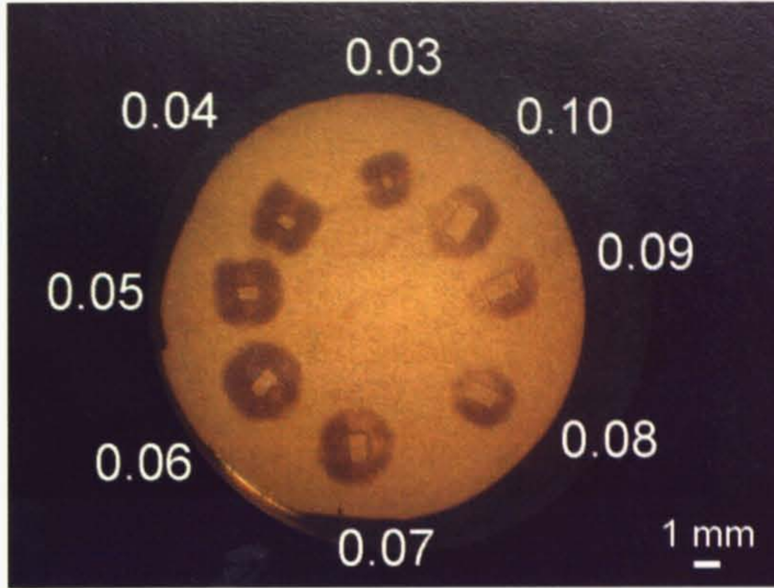

Figure 2.10: The profiles of the laser spots on the target surface. The white numbers indicate the calculated magnification of each spot.

magnification of the images (M_{act}) in comparison with the calculated values (M_{cal}). Though the actual magnification is slightly larger than the calculated value, we could obtain well-defined sharp images with different magnification on the target surface inside the chamber. The maximum energy density we obtained is above 20 J/cm^2 which is an order of magnitude higher than the typically employed energy density for PLD.

2.4 Summary

In order to examine the effect of the laser parameter, spot size S and fluence E, we have introduced a new optics system. We performed the ray tracing calculation with matrix technique. We constructed the optical system based on the matrix calculation and obtained the sharp laser spots whose magnification are easily controlled with considerable accuracy and reproducibility. We realized the high energy density of 20 J/cm^2 at the target surface.

M_{cal}	Length (mm)	Width (mm)	Area (mm^2)	M_{act}
0.03	0.775	0.500	0.00388	0.052
0.04	0.875	0.475	0.00416	0.058
0.05	0.975	0.575	0.00561	0.065
0.06	1.06	0.650	0.00691	0.071
0.07	1.28	0.750	0.00956	0.085
0.08	1.40	0.800	0.0112	0.093
0.09	1.58	0.875	0.0138	0.105
0.10	1.73	0.913	0.0157	0.115

Table 2.1: The comparison between the calculated and the experimentally measured values, size and magnification.

Bibliography

[1] T. Ohnishi, M. Lippmaa, T. Yamamoto, S. Meguro and H. Koinuma, Appl. Phys. Lett. **87**, 241919 (2005).

[2] F. X. Wagner, M. Scaggs, A. Koch, H. Endert, H. M. Christen, L. A. Knauss, K. S. Harshavardhan and S. M. Green, Appl. Surf. Sci. **127-129**, 477 (1998).

[3] K. Hallbach, Am. J. Phys. **32**, 90 (1964).

Chapter 3

Homoepitaxial films of $SrTiO_3$

3.1 Introduction

Homoepitaxy is a class of epitaxy in which the deposition material is identical to the substrate material. Since this growth mode is relatively simple from thermodynamic, chemical and structural points of view (compared with heteroepitaxy, in which the deposition material is different from the substrate material), it is instructive to study the characteristic of the homoepitaxial films in order to verify the effect of growth parameters. Homoepitaxial films of $SrTiO_3$ have been studied by several growth techniques such as MBE [1], radio frequency sputtering [2] and PLD [3, 4, 5, 6]. Especially PLD grown homoepitaxial films of $SrTiO_3$ have been intensively studied. The first feature is an elongation of the c-axis lattice constant despite homoepitaxy. As shown in Fig. 3.1(A), the film peaks clearly appear lower angle side of the substrate peaks. The origin of this elongation has not yet been explained well. It is often ascribed to the doping of impurities in the film [7], oxygen vacancies in the films [8] or off-stoichiometry of the cation ratio [Sr]/[Ti] [6]. The second feature is introduction of oxygen vacancies into the films during deposition at high growth temperature in low oxygen partial pressure conditions. As mentioned, these vacancies are known as electron donating dopants. Thus, the homoepitaxial films become conductors as shown in Fig. 3.1(B). The reported carrier density is typically the order of 10^{21} cm^{-3} [9]. Since these features are macroscopically observable features, we regarded them as powerful clues to study the growth dynamics of homoepitaxial films of $SrTiO_3$.

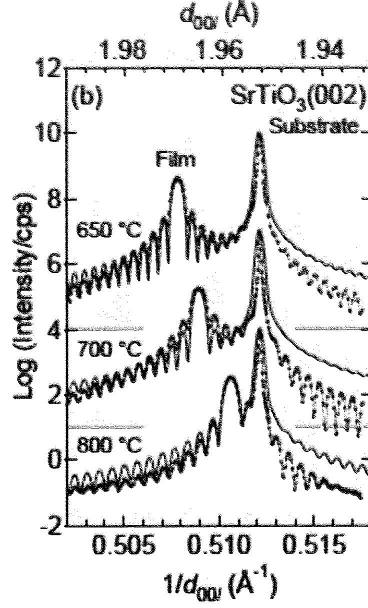

Figure 3.1: θ-2θ x-ray diffraction patterns near the (002) Bragg condition for homoepitaxial $SrTiO_3$ films grown in 1.0×10^{-6} Torr (650 °C and 700 °C) and 1.0×10^{-5} Torr (800 °C).

3.2 Experiments

$SrTiO_3$ films were grown by PLD in an ultra-high vacuum chamber whose base pressure is below $5.0{\times}10^{-8}$ Torr. A single crystal $SrTiO_3$ target was placed inside the chamber and irradiated with KrF excimer laser ($h\nu$ = 248 nm). We used commercially available atomically flat $SrTiO_3$ (100) substrates. After washed ultrasonically with acetone and ethanol, the substrate was mounted on an inconel holder with Pt paste. In order to remove the carbon contaminations on the surface and atomically reconstruct the surface, we performed a pre-annealing process at 900 °C in $1.0{\times}10^{-5}$ Torr for 30 min. We deposited homoepitaxial $SrTiO_3$ films by varying the laser spot size S and fluence E at the target surface, and growth temperature (Tg), while fixing the repetition rate at 4 Hz, the oxygen partial pressure (Po_2) at $1.0{\times}10^{-6}$ Torr and the target-substrate distance at 5 cm. After deposition the sample was cooled at a rate of 50 °C/min keeping Po_2 at $1.0{\times}10^{-6}$ Torr. We measured the c-axis lattice constant of grown films by x-ray diffraction (XRD) and transport properties by physical property measurement system (PPMS) from 300 K to 5 K. The electrical contact was made by wire bonding to evaporated Al electrodes.

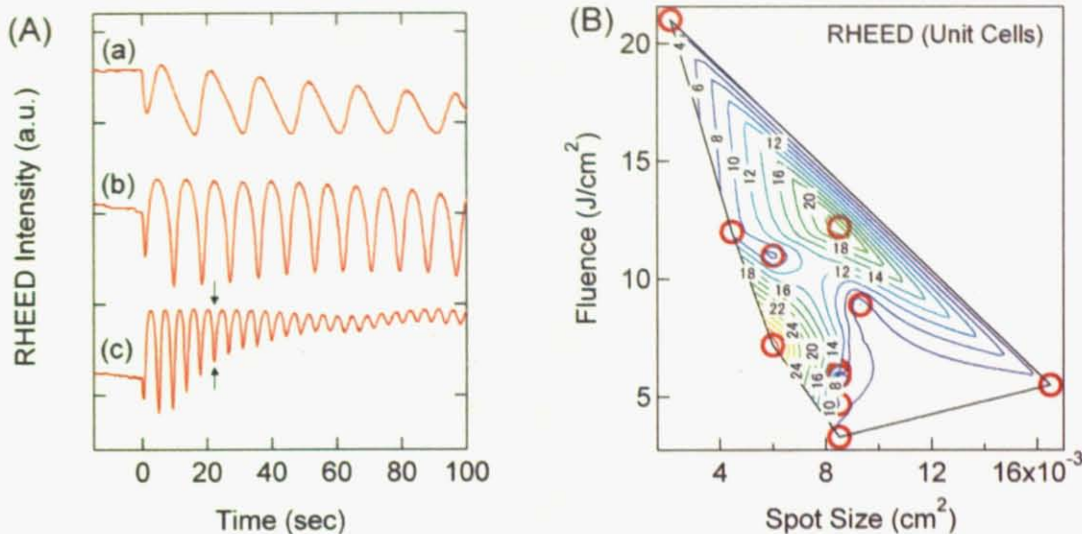

Figure 3.2: (A) RHEED intensity oscillations during homoepitaxial $SrTiO_3$ growth at 700 °C in 1.0×10^{-6} Torr with several laser parameters as (a) $S = 6.0 \times 10^{-3}$ cm² and $E = 11$ J/cm², (b) $S = 8.5 \times 10^{-3}$ cm² and $E = 12.2$ J/cm² and (c) $S = 16.5 \times 10^{-3}$ cm² and $E = 5.5$ J/cm². (B) Contour map of the number of unit cells for which half the RHEED oscillation amplitude is lost.

3.3 Results and discussion

3.3.1 Laser parameter effects

First, we fixed the growth conditions at 700 °C and in 1.0×10^{-6} Torr and varied the laser fluence E and spot size S. Figure 3.2(A) shows RHEED intensity oscillations of (a) $S = 6.0\times10^{-3}$ cm² and $E =$ 11 J/cm², (b) $S = 8.5\times10^{-3}$ cm² and $E = 12.2$ J/cm² and (c) $S = 16.5\times10^{-3}$ cm² and $E = 5.5$ J/cm². As mentioned, each oscillation corresponds to the construction of one unit cell of $SrTiO_3$. Figure 3.2(B) is a contour plot of the number of unit cells for which the amplitude of RHEED intensity oscillation is half of initial one, indicated by arrows of oscillation (c) in Fig. 3.2(A), as functions of laser parameters. Figure 3.3 is a contour plot of the deposition rate, defined as the required number of the pulses to deposit one monolayer, as functions of spot size S and fluence E. This result shows a tendency that smaller spot size S correspond to slower deposition rate. Moreover, we found that the deposition rate depends on rather spot size S than on fluence E. This tells us that the density of ablated adatoms on the substrate surface is mainly dominated by spot size S, namely, the size of plume profile is a strong function of the spot size S.

Figure 3.4(A) shows the θ-2θ XRD pattern near the (002) Bragg condition for 1000 Å thick films

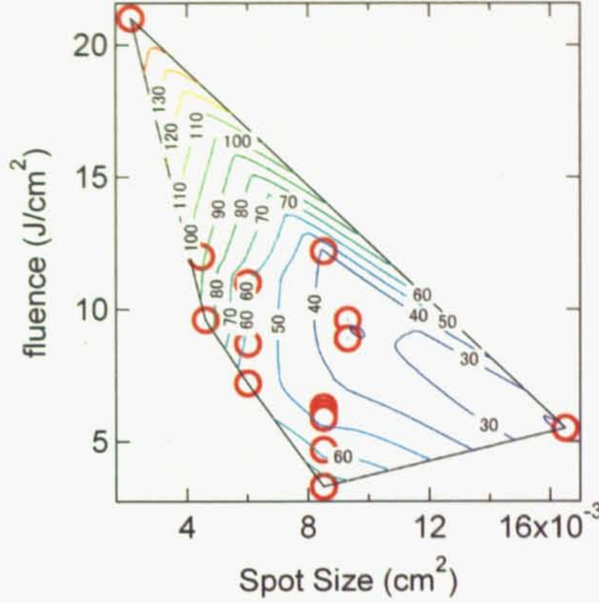

Figure 3.3: Contour map of deposition rate as functions of laser spot size S and fluence E.

grown with (a) $S = 6.0\times10^{-3}$ cm^2 and $E = 8$ J/cm^2, (b) $S = 8.5\times10^{-3}$ cm^2 and $E = 6.3$ J/cm^2 and (c) $S = 9.3\times10^{-3}$ cm^2 and $E = 8.9$ J/cm^2. We observed that the film peaks appeared the lower angle side of the substrate peak as reported [7], with the Laue fringes which indicates homogeneous thickness distribution of the films and sharp interface between the film and the substrate. We can determine the thickness of the films d by these fringe peak positions. From the Bragg equation, we write for scattering from interface:

$$\begin{cases} 2d\sin\theta_1 &= n_1\lambda \\ 2d\sin\theta_2 &= n_2\lambda \\ & \vdots \end{cases} \tag{3.1}$$

where, θ_1, θ_2, $\cdots$ are the angular positions of the peaks, n_1, n_2, $\cdots$ are characteristic integers. Thus,

$$d = \frac{(n_1 - n_2)\lambda}{2(\sin\theta_1 - \sin\theta_2)} \tag{3.2}$$

From the two adjacent Laue fringes indicated by arrows in Fig. 3.4(A), we can evaluate thickness of the film as 896 Å which is less than RHEED estimation (1000 Å). To consider this difference, we calculated the monitoring area of RHEED and XRD. For RHEED, we approximated that a diameter of

RHEED beam is 0.25 mm which is that of aperture and no divergence. An incident angle of RHEED beam in our equipment is about 3°. Thus, the monitoring area of RHEED (S_{RHEED}) is

$$S_{\text{RHEED}} = \pi \times \frac{0.25}{2} \times \frac{1}{2}\frac{0.25}{\sin(3^{\circ})} = 0.942 \ (\text{mm}^2) \tag{3.3}$$

For XRD, we approximated that x-ray beam dimension is same as the slit size which is 1 × 6 mm. An incident angle of x-ray is about 23°, which yield

$$S_{\text{XRD}} = 6 \times \frac{1}{\sin(23^{\circ})} = 15 \ (\text{mm}^2) \tag{3.4}$$

As seen, the monitoring area of XRD is fifteen times larger than that of RHEED and comparable in size to the samples (5 × 5 mm^2). Thus, we speculated that thickness distribution of the films would be in error of about 10 %.

It is clearly seen that the film peaks appear at different positions by changing the laser parameters even under fixed thermodynamical growth conditions as shown in Fig. 3.4(A). C-axis length is plotted in Figure 3.4(B) as functions of laser spot size S and fluence E. For the film grown by relatively small spot size S and high fluence E, the film peak is most separated from that of the substrate. It is reasonable to speculate that the contribution of laser fluence might be the kinetic effect and that of spot size might be deposition.

The transport properties of homoepitaxial films grown at 700 °C and in 1.0 $\times 10^{-6}$ Torr with various laser parameters are shown in Fig. 3.5. Figure 3.5(A) shows the temperature dependent resistivity measured in four-probe method. In spite of the different laser parameters, all the samples show quite similar conducting properties. The temperature dependent Hall mobility shows also similar behavior as shown in Fig. 3.5(B). Above 100 K, the mobility is approximated by straight line of $T^{-3.4}$ and finally reaches 20,000 cm^2/Vs at 5 K. These results are quite similar to previous work on the bulk reduced $SrTiO_{3-\delta}$ [10].

Figure 3.6 is a contour plot of the carrier density as functions of laser parameters. Most films have fairly high carrier density of the order of 10^{21} cm^{-3} except the films grown with smallest spot size 2.1 $\times$ 10^{-3} cm^2 and highest fluence 21 J/cm^2 which shows high resistivity. In general, a larger spot area

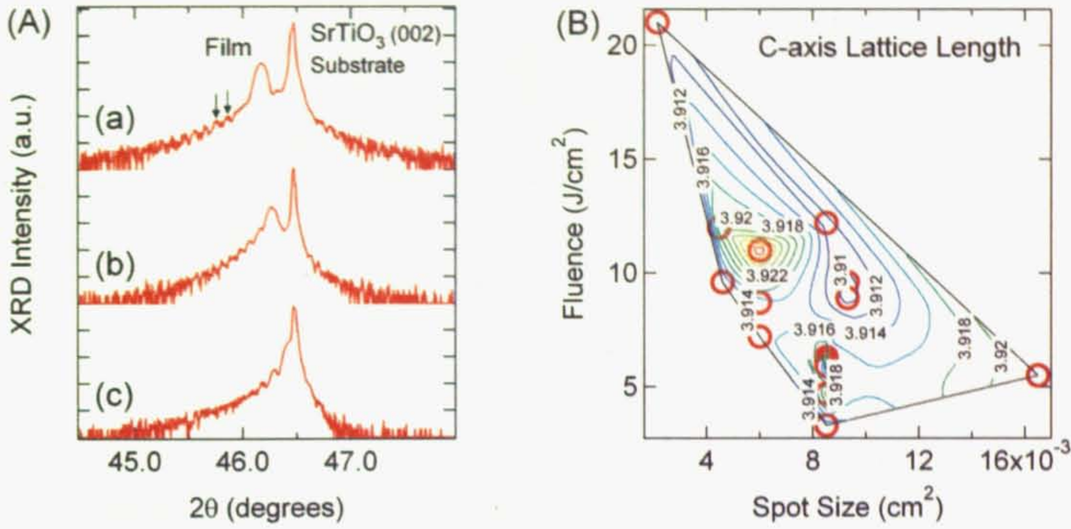

Figure 3.4: (A) $\theta - 2\theta$ x-ray diffraction patterns near the (002) Bragg condition for the films grown at 700 °C in 1.0×10^{-6} Torr with (a) $S = 6.0\times10^{-3}$ cm^2 and $E = 8$ J/cm^2, (b) 8.5×10^{-3} cm^2 and $E = 6.3$ J/cm^2 and (c) $S = 9.3\times10^{-3}$ cm^2 and $E = 8.9$ J/cm^2. (B) Coutour map of the c-axis lattice length as functions of laser spot size S and fluence E.

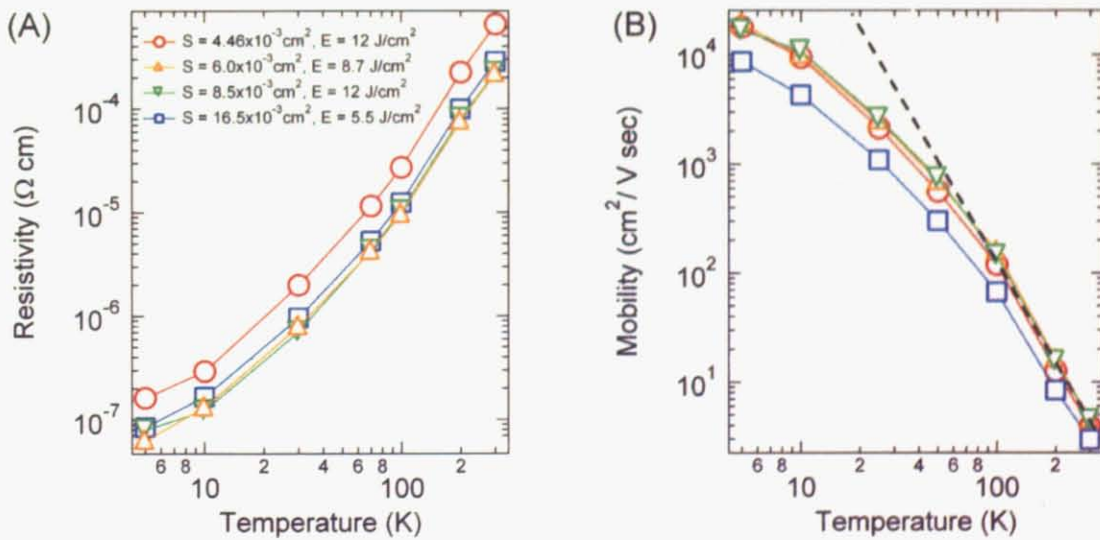

Figure 3.5: (A) Temperature dependent resistivity for films grown with $S = 4.46\times10^{-3}$ cm^2 and $E = 12$ J/cm^2 (red circle), $S = 6.0\times10^{-3}$ cm^2 and $E = 8.7$ J/cm^2 (orange triangle), $S = 8.5\times10^{-3}$ cm^2 and $E =$ 12.2 J/cm^2 (grren triangle) and $S = 16.5\times10^{-3}$ cm^2 and $E = 5.5$ J/cm^2 (blue square). (B) Temperature dependent mobility of same samples. The dashed line shows the approximate line of the form of $\mathrm{T}^{-3.4}$.

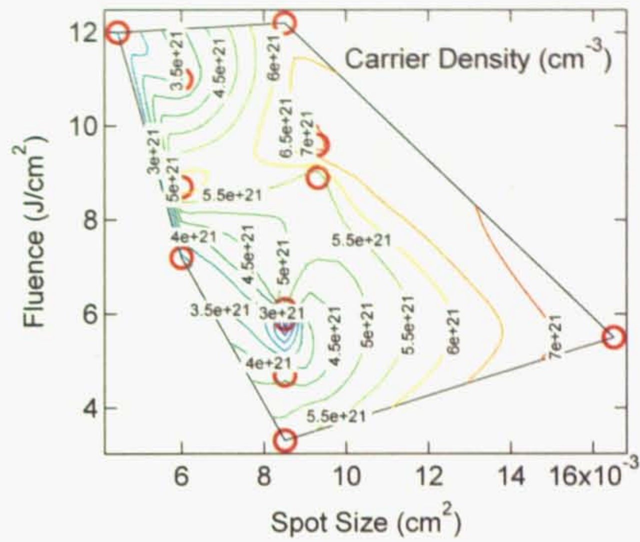

Figure 3.6: Contour map of the room temperature (300 K) carrier density as a function of laser spot size S and fluence E.

introduced higher carrier density, which might be related to deposition time scale.

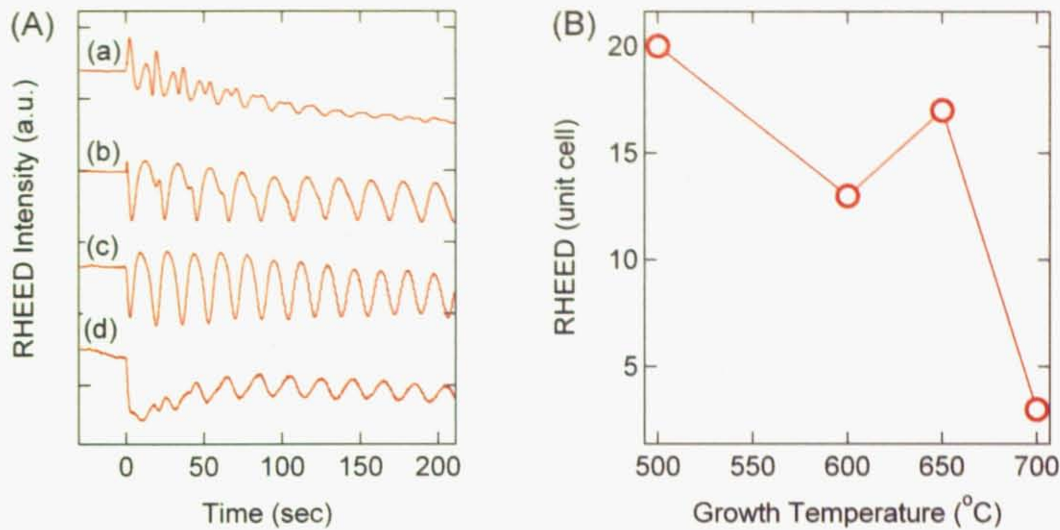

Figure 3.7: (A) RHEED intensity ocsillations during homoepitaxial $SrTiO_3$ growth at 700 °C (a), 650 °C (b), 600 °C (c) and 500 °C (d) 1.0×10^{-6} Torr with fixed laser parameters as $S = 6.0\times10^{-3}$ cm^2 and E = 11 J/cm^2. (B) The number of unit cells for which half the RHEED oscillation amplitude is lost as a function of growth temperature.

3.3.2 Growth temperature effects

As a next step, we varied growth temperature from 700 °C to 500 °C while fixing the laser parameters as the spot size $S = 6.0\times10^{-3}$ cm^2 and fluence E = 11 J/cm^2. Figure 3.7(A) shows RHEED intensity oscillations during deposition at (a) 700 °C, (b) 650 °C, (c) 600 °C and (d) 500 °C. To find the optimal condition of layer-by-layer growth mode, we plotted the number of unit cells for half amplitude of initial oscillation as shown in Fig. 3.7(B). As seen, lower growth temperature resulted in larger number of unit cells. However, initial recovery ratio and degree of oscillation amplitude is much better for the samples grown at 650 °C or 600 °C than 500 °C. For 700 °C samples, the oscillation diminished quickly.

Figure 3.8(A) shows the θ-2θ XRD pattern near the (002) Bragg condition for 500 Å thick films grown at 700 °C (red line), 675 °C (orange line), 650 °C (yellow line), 625 °C (green line), 600 °C (blue line) and 500 °C (purple line). Clearly seen is the systematic departure of the film peaks away from the substrate peak as the growth temperature decreases. We plotted c-axis lattice constant as a function of the growth temperature in Fig. 3.8(B). Between 600 °C and 500 °C, separation of peaks suddenly became significant.

Figure 3.9(A) and (B) show the temperature dependent resistivity and mobility for conducting films

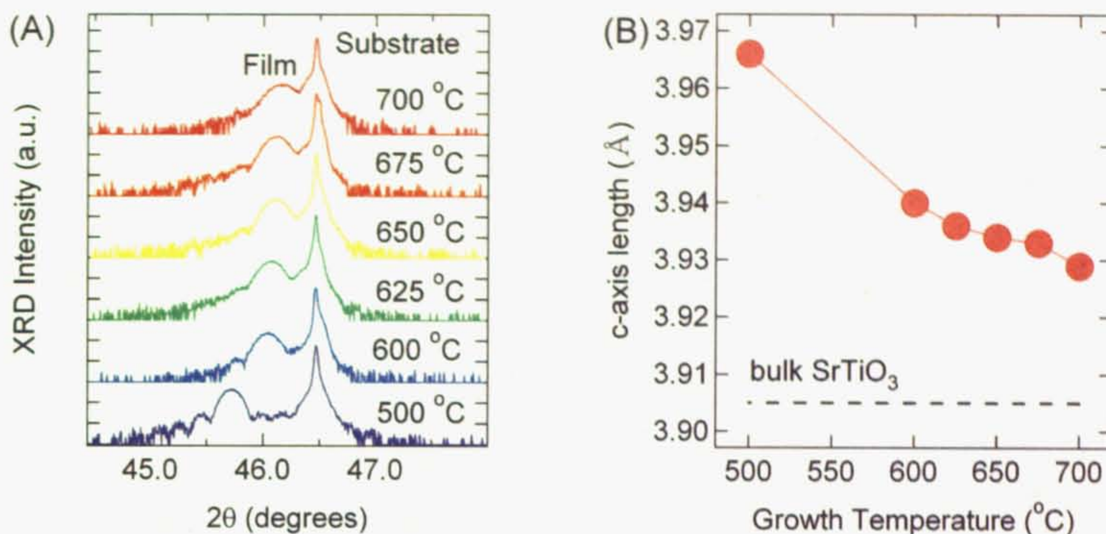

Figure 3.8: (A) $\theta - 2\theta$ x-ray diffraction patterns near the (002) Bragg condition for the films grown at 700 °C (red), 675 °C (orange), 650 °C (yellow), 625 °C (green), 600 °C (blue) and 500 °C (purple). (B) The c-axis lattice length as a function of growth temperature.

grown at 800 °C (red circle), 700 °C (orange circle), 675 °C (green circle), 650 °C (blue circle) and 625 °C (purple circle). We observed the clear metal-insulator transition in the film grown at 625 °C. The room temperature carrier density is plotted in Fig. 3.10 as a function of growth temperature. We observed that all the conducting samples have 10^{21} cm^{-3} order of carrier density and sharp metal-insulator transition around Tg=625 °C. According to [11], we found that the activation energy for the Tg dependence of the room temperature carrier density at high Tg region is about 0.42 eV, which is 1/3 of the reported value. We found transition growth temperature around Tg=625 °C in c-axis lattice length and electrical properties. Qualitatively, such sharp transition would be explained by competition of kinetics of surface crystallization and oxidation [9]. However, quantitative interpretation has not yet completed.

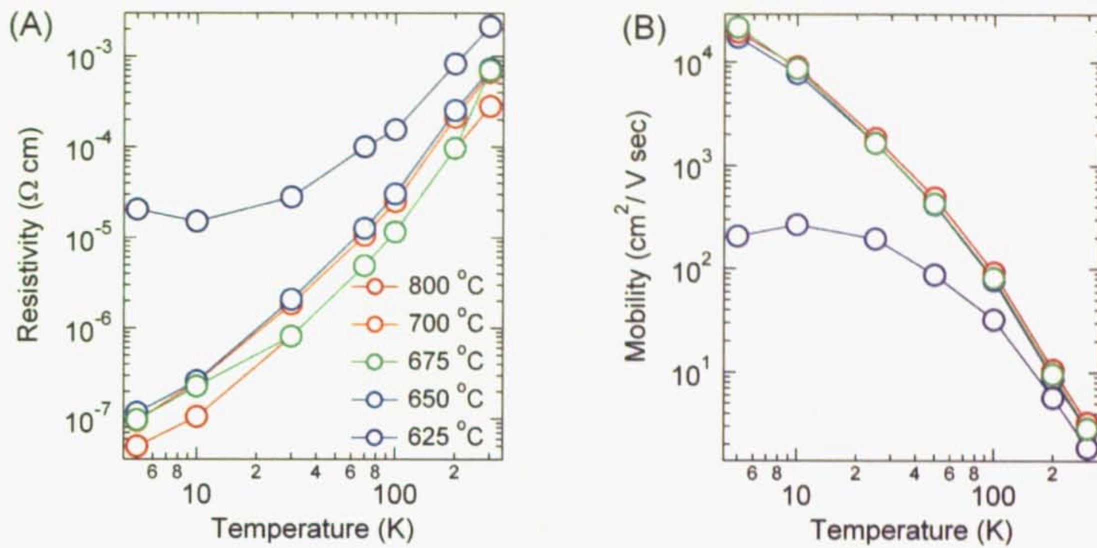

Figure 3.9: (A) The temperature dependendent resistivity and (B) Hall mobility for samples grown at 800 °C (red circle), 700 °C (orange circle), 675 °C (green circle), 650 °C (blue circle) and 625 °C (purple circle).

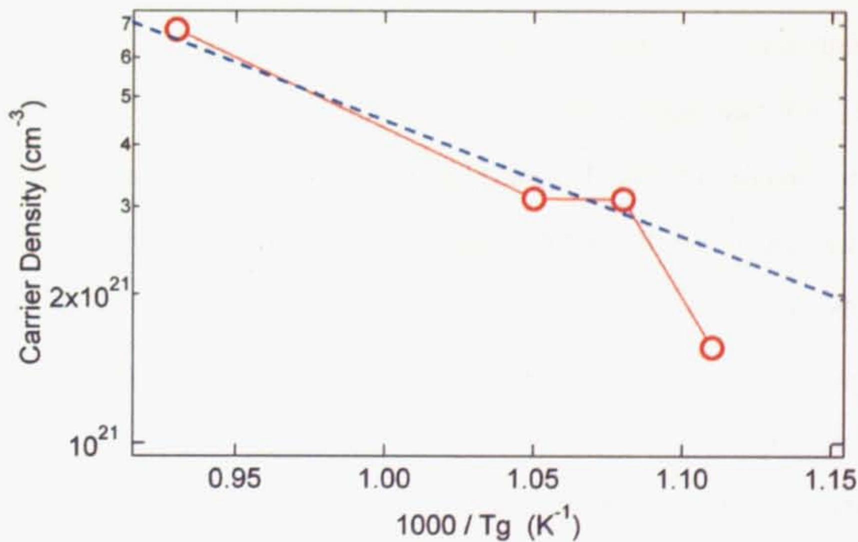

Figure 3.10: The room temperature (300 K) carrier density as a function of growth temperature. The dashed line shows the approximation line of the form of Arrhenius function : $n_{300K} = C\exp(-E_{ox}/k_BT_g)$. The slope gives the activation energy of surface oxidation.

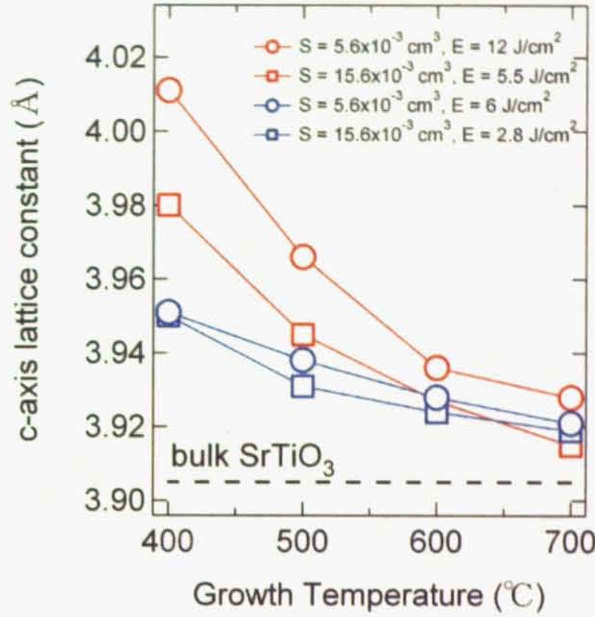

Figure 3.11: The c-axis lattice length as a function of the growth temperature. The red circles corresponds to $S = 5.6\times10^{-3}$ cm^2 and $E = 12$ J/cm^2, the blue circles to $S = 5.6\times10^{-3}$ cm^2 and $E = 6$ J/cm^2, the red squares to $S = 15.6\times10^{-3}$ cm^2 and $E = 5.5$ J/cm^2 and $S = 15.6\times10^{-3}$ cm^2 and $E = 2.8$ J/cm^2.

3.3.3 Laser parameters and growth temperature

We also fabricated the series of samples at different growth temperatures with the following laser parameters: $S = 5.6\times10^{-3}$ cm^2 and $E = 12$ J/cm^2 (red circle), $E = 6$ J/cm^2 (blue circle), $S = 9.56\times10^{-3}$ cm^2 and $E = 7.7$ J/cm^2 (red triangle), $E = 3.9$ J/cm^2 (blue triangle) and $S = 15.6\times10^{-3}$ cm^2 and $E = 5.5$ J/cm^2 (red square), $E = 2.8$ J/cm^2 (blue square). Figure 3.11 shows c-axis lattice constant as a function of growth temperature. Samples grown with lower fluence E for each spot size S show similar behavior, slowly increasing as the growth temperature decreases. On the other hand, at higher fluence the films show relatively large expansion as the growth temperature decrease. It is noteworthy that higher fluence enlarges the c-axis lattice constant at lower growth temperature. In general, it is recognized that increasing fluence is equivalent to increase in the growth temperature since diffusion of adatoms on the substrate surface would be increased. Our results show opposite trend and indicate that kinetic energy of the impinging particle would not be compatible with the surface diffusion energy directly.

Figure 3.12(A) shows the temperature dependent resistivity for the samples grown at 700 °C in which all the samples show metallic behaviors in spite of a variety of laser parameter. In contrast, it is

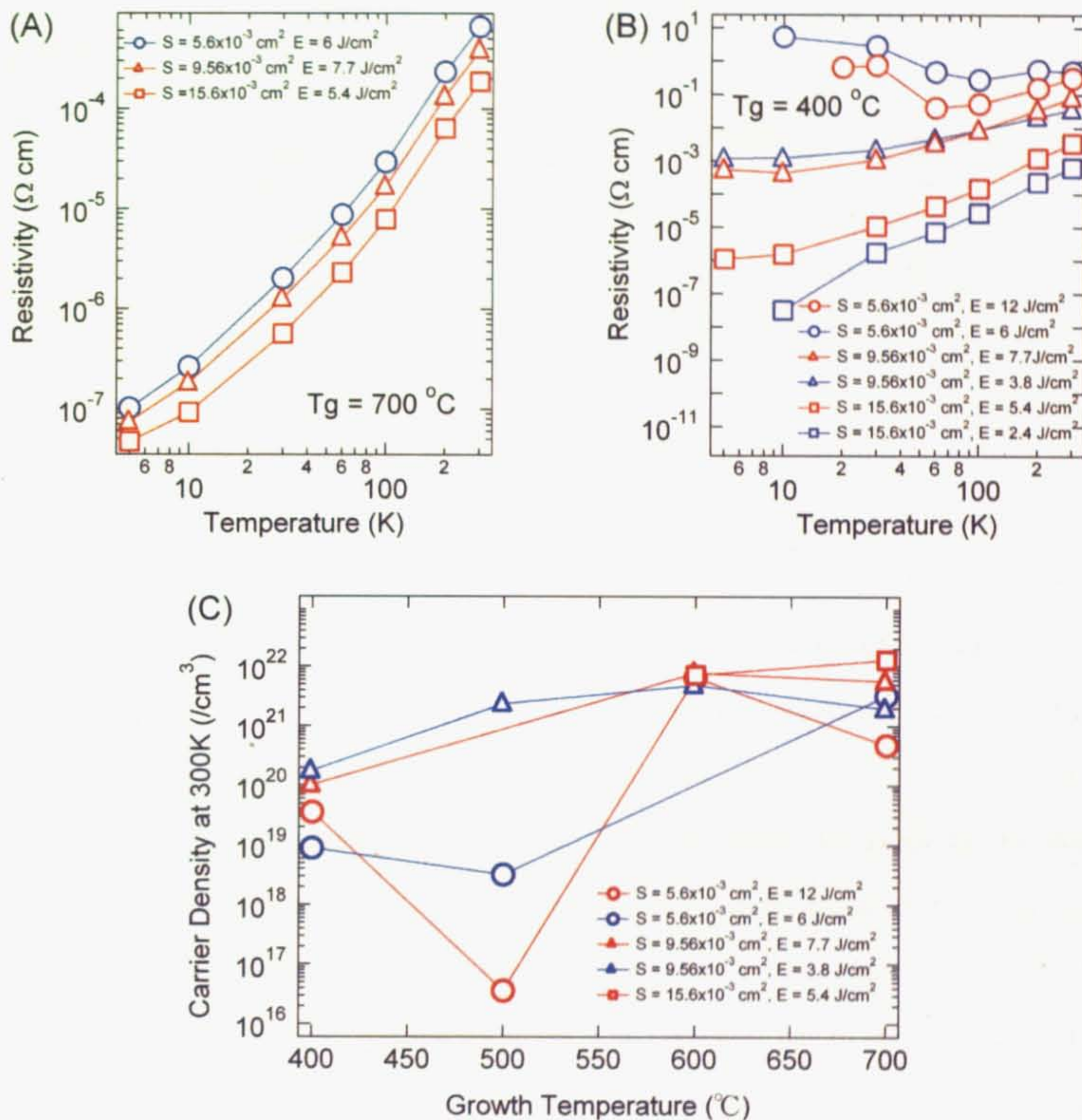

Figure 3.12: The spot size and the energy density dependence of the resistivity of the films grown at 700 °C (A) and 400 °C (B) and the room temperature carrier density as a function of the growth temperature (C). The blue circles correspond to $S = 5.6 \times 10^{-3}$ cm^2 and $E = 6.1$ J/cm^2, the red circles to $S = 5.6 \times 10^{-3}$ cm ^{2} and $E = 11.8$ J/cm^2, the blue triangles to $S = 9.56 \times 10^{-3}$ cm ^{2} and $E = 3.8$ J/cm^2, the red triangles to $S = 9.56 \times 10^{-3}$ cm ^{2} and $E = 7.7$ J/cm^2, the blue squares to $S = 15.6 \times 10^{-3}$ cm ^{2} and $E = 2.4$ J/cm^2 and the red squares to $S = 15.6 \times 10^{-3}$ cm ^{2} and $E = 5.4$ J/cm^2.

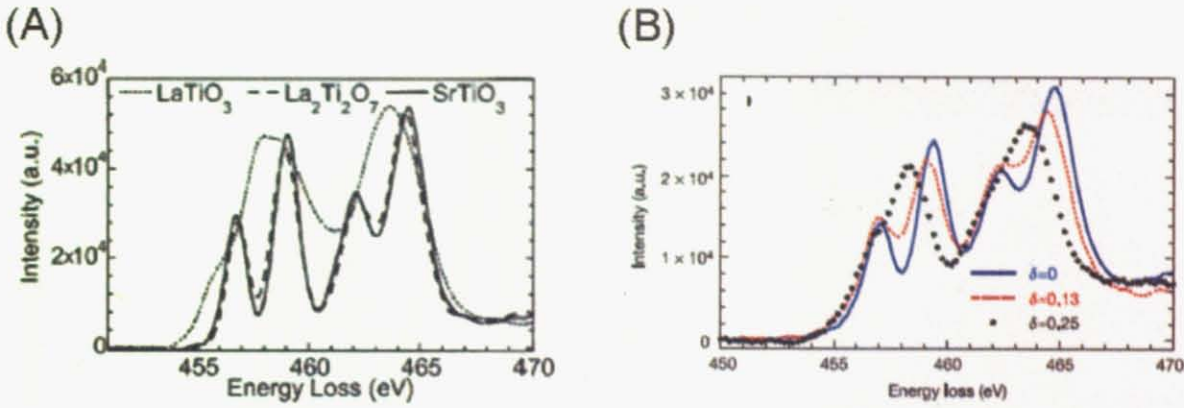

Figure 3.13: (A) Ti $L_{2,3}$ electron energy-loss spectra taken from the $LaTiO_3$ film, $La_2Ti_2O_7$ film, and $SrTiO_3$ substrate. Adopted from Ref. [12]. (B) The Ti $L_{2,3}$ shifts from a Ti^{4+} to Ti^{3+} valence of oxygen deficient $SrTiO_{3-\delta}$, for $\delta = 0$, 0.13 and 0.25. Adopted from Ref. [15].

remarkable that the samples grown at 400 °C show the systematic transition from metallic to insulator by decreasing spot size. As far as we investigated, spot size is far more dominant factor of electrical properties of the films than fluence. Figure 3.12(C) shows the room temperature carrier density for sample grown with various laser parameters as a function of growth temperature. Samples grown with small spot size show distinguishable dropping of the carrier density between 600 °C and 500 °C and the others show gently sloping as growth temperature decrease.

Electron energy-loss spectroscopy (EELS) tells information about the energy lost by electrons as they penetrate through the samples. The most valuable loss features are absorption edges caused by electronic transitions of atomic core levels. Figure 3.13(A) shows reference EELS spectra for Ti^{4+} and Ti^{3+} [12]. The $La_2Ti_2O_7$ and $SrTiO_3$ spectra shows close agreement due to the Ti^{4+} state [13] and the $LaTiO_3$ spectra shows the Ti^{3+} state [14]. Figure 3.13(B) shows the Ti-L edge spectra of stoichiometric and oxygen deficient $SrTiO_3$ [15] . The blue line shows the Ti^{4+} spectra taken from stoichiometric $SrTiO_3$, the red line from moderately reduced $SrTiO_3$ and the black line from heavily reduced $SrTiO_3$. The systematic change of the shape of spectra from Ti^{4+} to Ti^{3+} valence state is observed as reduction advances. Since an oxygen vacancy nominally produces two electrons to the Ti d band, the Ti^{3+} state is evidence of oxygen vacancies.

An EELS scan crossing a homoepitaxial $SrTiO_3$ film is shown in Fig. 3.14. The sample was grown at 750 °C in 1.0×10^{-6} Torr with laser parameters of $S = 6.0\times10^{-3}$ cm^2 and $E = 11$ J/cm^2. It has 500

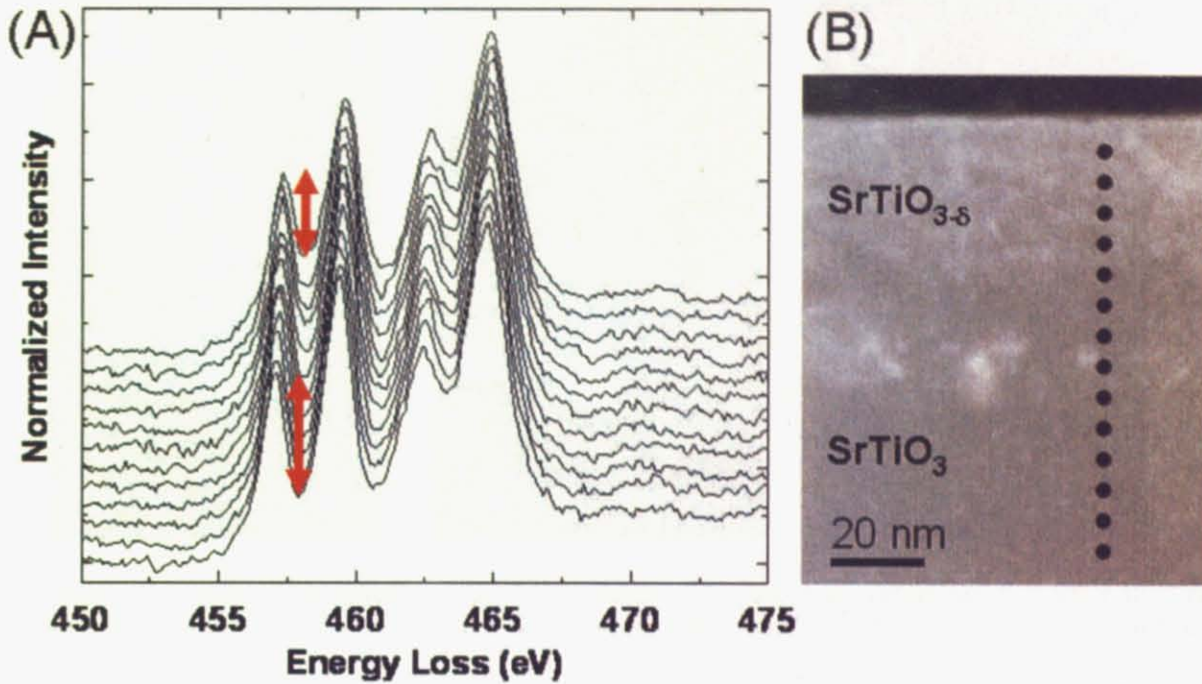

Figure 3.14: (A) Ti $L_{2,3}$ electron energy-loss spectra recorded across a homoepitaxial $SrTiO_3$ film. (B) The electron scanning position for spectra measurement. Adopted from Ref. [16].

Å thickness and carrier density of 1.9×10^{21} cm^{-3}. In Fig. 3.14(A), only small changes in the spectra structure was observed as indicated by red arrows. This small deviation, reduction of the depth of valley, would be ascribed to the onset of Ti^{3+} admixture. Although the carrier density of this sample ($\sim 2\times10^{21}$ cm^{-3}) is close to that shows red spectra line in Fig. 3.13(A) ($\sim 4\times10^{21}$ cm^{-3}), the deviation from Ti^{4+} spectra is small. Thus, we guessed that the oxygen vacancies would diffuse into the substrate and exists widely in the samples. As a result, the actual carrier density would be much lower than the calculated value. This speculation can also explain the lack of contrast in ADF image in Fig. 3.14(B) compared with previous results in Fig. 1.7(A) and deviation of activation energy of surface oxidation.

The result of Fig. 3.12(B) would reflect the profile of the plume, which strongly depends on the dimension of the laser spot on the target. As mentioned in Chap. 1, the spatial distribution of the plume is well described by means of the gas dynamics theory [17, 18, 19, 20, 21].

In order to visualize the plume expansion, we took a series of photographs of the plume with various laser parameters as shown in Fig. 3.15. We found that the profile of the plumes show the systematic change perpendicular to the target surface with increasing the spot size. The small spot size corresponds

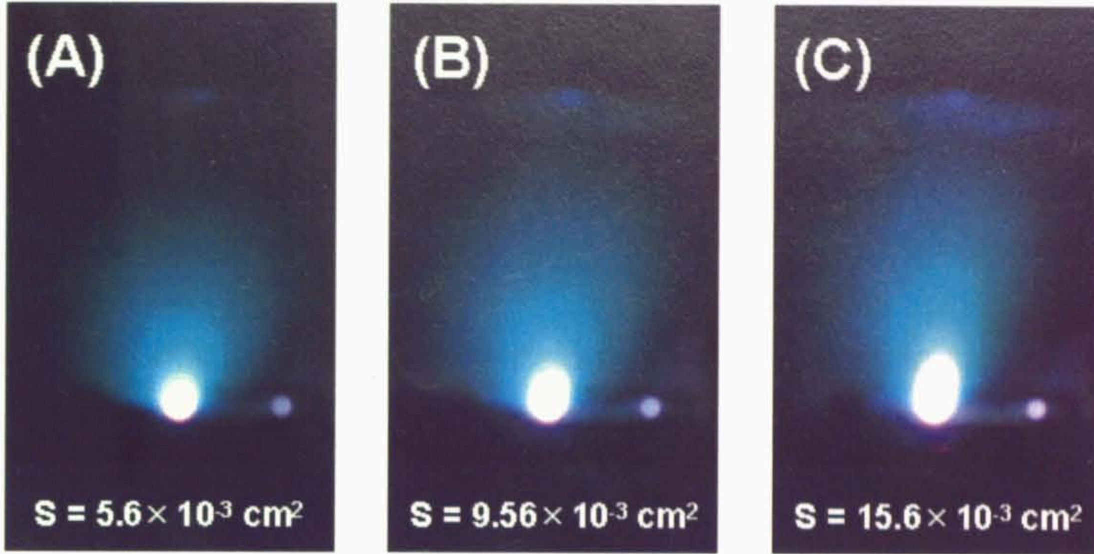

Figure 3.15: The series of the photographs of the plumes. The laser parameters are $S = 5.6 \times 10^{-3}$ cm ^{2} and $E = 10.6$ J/cm^2 (A), $S = 9.56 \times 10^{-3}$ cm ^{2} and $E = 7.9$ J/cm^2 (B) and $S = 15.6 \times 10^{-3}$ cm ^{2} and $E = 5.2$ J/cm^2 (C).

to the horizontally expanded distribution (Fig. 3.15(A),(B)), while the large spot size corresponds to the perpendicularly expanded distribution.

In order to estimate spot size dependence of the angular distribution of the plume, we utilized the approach of Kools *et al.* [22, 23]. In their approach, the evolution of the ablated plume is divided in three stages as shown in Fig. 3.16: (1) generation of the vaporized material, (2) one-dimensional expansion perpendicular to target surface for a distance Z, (3) following three dimensional expansion of the plume. In general, the point source evaporation has angular distribution $f(\theta)$ of the form of $\cos^p(\theta)$ and a film thickness profile $D(\theta)$ of the form of $\cos^{p+3}(\theta)$.

They obtained approximation of p in the case of a circular laser spot as

$$p = 3.9\Big(1 + 2\left(\frac{Z}{X}\right)^{1.2}\Big)^{3/4}\left(\frac{X}{Z}\right)^{1.2} \tag{3.5}$$

where X is a diameter of a circular spot and Z is a height of the plume at the onset of three-dimensional expansion, which is less simple for evaluation than X. However, it is reported that values of about 400 μm are found to give a reasonable prediction of experimental data. The assumption of $Z = 400$ μm enables to make a rough estimation of the angular distribution of an ablated plume. We used several

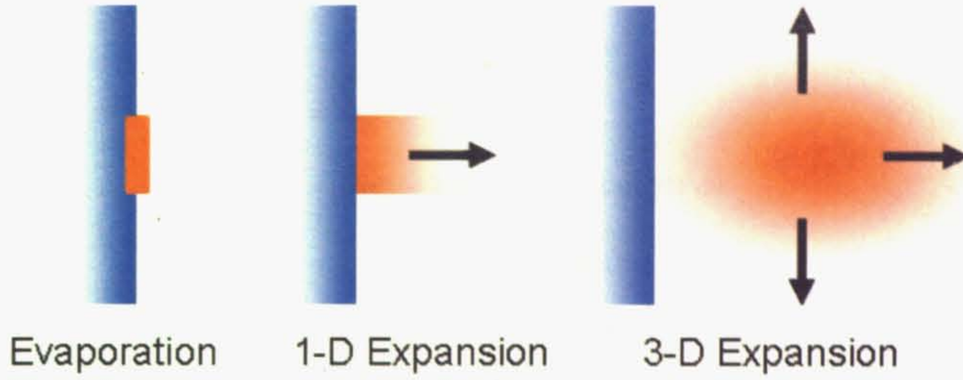

Figure 3.16: Schematic illustration of the expansion of the plume based on the hydrodynamical model. The plume is generated by ultrafast vaporization from a solid. The plume will at initial stage expand one-dimensionally and then transverse into three dimensional expansion.

spot sizes as 0.6×1.0 mm^2 (small), 0.75×1.3 mm^2 (middle) and 0.9×1.64 mm^2 (large). Although our spot shape is rectangular, for further calculations using this method, we assumed the circular spots with the diameters of 0.6 mm, 0.75 mm and 0.9 mm respectively. Substituting these approximate diameters for formula (3.1), we obtained values p of 11.5 for small spot, 13.8 for middle spot and 15.7 for large spot. Thus, angular distribution and the film thickness profiles of each spot size becomes,

$$\begin{cases} f(\theta)_{\mathrm{small}} \propto \cos^{11.5}(\theta) \\ f(\theta)_{\mathrm{middle}} \propto \cos^{13.8}(\theta) \\ f(\theta)_{\mathrm{large}} \propto \cos^{15.7}(\theta) \\ D(\theta)_{\mathrm{small}} \propto \cos^{14.5}(\theta) \\ D(\theta)_{\mathrm{middle}} \propto \cos^{16.8}(\theta) \\ D(\theta)_{\mathrm{large}} \propto \cos^{18.7}(\theta) \end{cases} \tag{3.6}$$

To compare thickness profiles, we assumed that $D(\theta)_{\mathrm{spot\ size}}=\mathrm{C}_{\mathrm{spot\ size}}\cos^{p+3}(\theta)$ and calculated the volume of deposited films.

The small amount of volume is obtained as follows,

$$\delta V = D(\theta) \times \delta S(\theta)$$

$$= D(\theta) \times 2\pi l \tan(\theta) \times l(\tan(\theta))' d\theta \quad (3.7)$$

$$= 2\pi l^2 D(\theta) \times \tan(\theta)(\tan(\theta))' d\theta \quad (3.8)$$

$$= 2\pi l^2 C \cos^{p+3}(\theta) \tan(\theta)(\tan(\theta))' d\theta \quad (3.9)$$

where l is a target-substrate distance. Thus, the total volume is

$$V = \int_0^{\frac{\pi}{2}} \delta V$$

$$= 2\pi l^2 C \int_0^{\frac{\pi}{2}} \cos^{p+3}(\theta) \tan(\theta)(\tan(\theta))' d\theta \quad (3.10)$$

$$= 2\pi l^2 C \int_0^{\frac{\pi}{2}} (\cos^2(\theta))^{\frac{p+3}{2}} \tan(\theta)(\tan(\theta))' d\theta \quad (3.11)$$

$$= 2\pi l^2 C \int_0^{\frac{\pi}{2}} \left(\frac{1}{1+\tan^2(\theta)}\right)^{\frac{p+3}{2}} \tan(\theta)(\tan(\theta))' d\theta \quad (3.12)$$

$$= 2\pi l^2 C \int_0^{\frac{\pi}{2}} \left(1+\tan^2(\theta)\right)^{-\frac{p+3}{2}} \tan(\theta)(\tan(\theta))' d\theta \quad (3.13)$$

$$= \left[\frac{1}{2(-\frac{p+3}{2}+1)}(1+\tan^2(\theta))^{(-\frac{p+3}{2}+1)}\right]_0^{\frac{\pi}{2}} \quad (3.14)$$

In our case, clearly $-\frac{p+3}{2} + 1 < 0$, therefore

$$V = -\frac{1}{2(-\frac{p+3}{2}+1)} \quad (3.15)$$

Substitution of p values into this formula yields,

$$\begin{cases} V_{\text{small}} = \dfrac{\pi l^2 C_{\text{small}}}{7.8} \\ V_{\text{middle}} = \dfrac{\pi l^2 C_{\text{middle}}}{8.9} \\ V_{\text{large}} = \dfrac{\pi l^2 C_{\text{large}}}{9.9} \end{cases} \quad (3.16)$$

In order to normalize the pre-exponential factors with respect to C_{small}, we made an assumption that

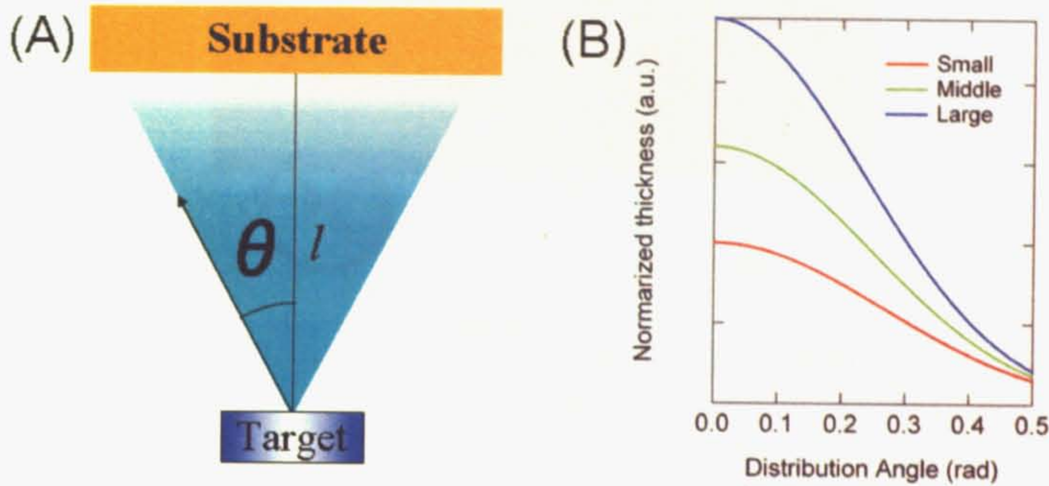

Figure 3.17: (A) Schematic illustration of deposition geometry. (B) Angular distribution of thickness of deposited material.

total volume of deposited material is in proportion to spot size with same fluence. Normalization of the pre-exponential factor with respect to C_{small} gives,

$$\begin{cases} \dfrac{C_{\mathrm{middle}}}{C_{\mathrm{small}}} = \dfrac{0.75 \times 1.3}{0.6 \times 1.0} \sim 1.6 \\ \dfrac{C_{\mathrm{large}}}{C_{\mathrm{small}}} = \dfrac{0.90 \times 1.6}{0.6 \times 1.0} \sim 2.4 \end{cases} \tag{3.17}$$

Assuming that C_{small} =1, the thickness profiles are given as.

$$\begin{cases} D(\theta)_{\mathrm{small}} = \cos^{14.5}(\theta) \\ D(\theta)_{\mathrm{middle}} = 1.6 \cos^{16.8}(\theta) \\ D(\theta)_{\mathrm{large}} = 2.4 \cos^{18.7}(\theta) \end{cases} \tag{3.18}$$

and shown in Fig. 3.17(B).

Considering the above results and discussions, one possible scenario, we speculated, was "re-sputtering effect" by impinging particles in plume. Sputtering is a physical process where atoms in the solid target material are ejected into the gas phase due to bombardment of the material by highly energetic ions. The principle mechanism of the sputtering is the momentum exchange between the energetic ions and atoms

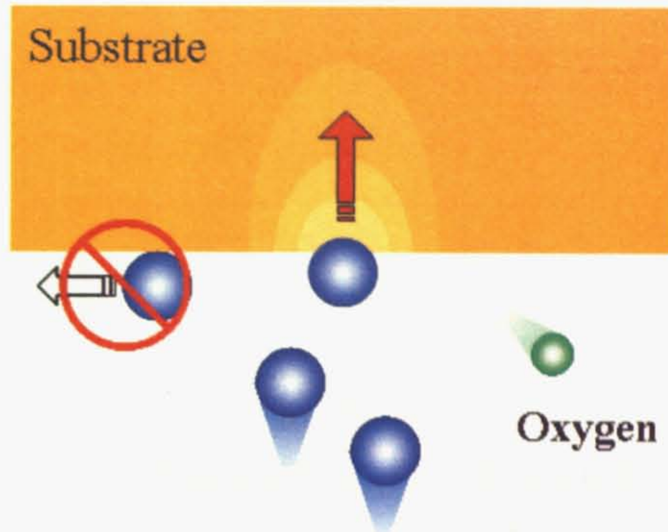

Figure 3.18: Schematic drawing of sputtering effects during deposition.

in the target material via collision process. It is generally recognized that deposition in ultrahigh vacuum conditions, resputtering of the deposited materials by bombardment of highly energetic particles during deposition is a rather common accident [24, 25, 26]. In Fig. 3.11, we found that laser fluence would not be equivalent to surface diffusion energy provided by growth temperature. It is, then, reasonable to speculate that kinetic energies of impinging particles enhanced by high fluence might propagate into the substrate and eject the atoms of bulk substrate as shown schematically in Fig. 3.18. It is reported that the plume created with high fluence above 5 J/cm^2 would include the highly excited ions with the energy of up to a few 100 eV [27]. Thus, these energetic ions are one of the candidates of inducing resputtering effects. It is reasonable to assume that the effect of sputtering depends on the density of the species in the plume. As described, a larger spot creates narrower angular distribution which results in a dense assemble of the energetic ions. Such difference of plume density would lead to the strong spot size dependence in resistivity of films shown in Fig 3.12. There are several reports on preferential sputtering of oxygen atoms from oxide compounds. González-Elipe *et al.* show preferential oxygen loss from TiO_2 by 3.5 keV Ar^+ ion sputtering [28]. For $SrTiO_3$, Henrich *et al.* reported the preferential sputtering of not only oxygen atoms but also strontium atoms (Sr) from the surface by 500 eV Ar ions bombardment [29]. In our case, removal of Sr atoms could also have happened. Such dislocations would enhance the diffusion of oxygen vacancies deeply into the bulk substrate.

Bibliography

[1] M. Watamori, K. Oura and T. Nakamura, J. Vac. Sci. Technol. A **13(3)**, 1293 (1995).

[2] H. Y. Lee, C. H. Hsu, Y. W. Hsieh and H. J. Liu, Thin Solid Films **469-470**, 327 (2004).

[3] H. Y. Lee, W. D. Chang, C. H. Hsu, K. S. Liang, J. Y. Lee, J. Y. Juang, K. H. Wu, T. M. Uen and Y. S. Gou, Thin Solid Films **418**, 163 (2002).

[4] D. W. Kim, D. H. Kim, B. S. Kang, T. W. Noh, S. Shin and Z. G. Khim, Physica C **313**, 246 (1999).

[5] J. H. Song and Y. H. Jeong, Solid State Commun. **125**, 563 (2003).

[6] T. Ohnishi, M. Lippmaa, T. Yamamoto, S. Meguro and H. Koinuma, Appl. Phys. Lett. **87**, 241919 (2005).

[7] J. P. Contour, D. Ravelosona, C. Sant, C. Fretighy, C. Dolin, J. Rioux, P. Auvray and J. Caulet, J. Cryst. Growth **141**, 141 (1994).

[8] E. J. Tarsa, E. A. Hachfeld, F. T. Quinlan, J. S. Speck and M. Eddy, Appl. Phys. Lett. **68**, 490 (1996).

[9] A. Ohtomo and H. Y. Hwang, unpublished.

[10] H. P. R. Frederikse, W. R. Thurber and W. R. Hosler, Phys. Rev. **134**, A442 (1964).

[11] X. D. Zhu, W. Si, X. X. Xi and Q. Jiang, Appl. Phys. Lett. **78**, 460 (2001).

[12] A. Ohtomo, D. A. Muller, J. L. Grazul and H. Y. Hwang, Appl. Phys. Lett. **80**, 3922 (2002).

[13] Z. Zhang, W. Sigle and M. Rühle, Phys. Rev. B **66**, 094108 (2002).

[14] M. Abbate, F. M. F. de Groot, J. C. Fuggle, A. Fujimori, Y. Tokura, Y. Fujishima, O. Strebel, M. Domke, G. Kaindl, J. van Elp, B. T. Thole, G. A. Sawatzky, M. Sacchi and N. Tsuda, Phys. Rev. B **44**, 5419 (1991).

[15] D. A. Muller, N. Nakagawa, A. Ohtomo, J. L. Grazul and H. Y. Hwang, Nature **430**, 657 (2004).

[16] L. Fitting and D. A. Muller, unpublished.

[17] A. Casavola, G. Colonna and M. Capitelli, Appl. Surf. Sci. **208-209**, 85 (2003).

[18] T. E. Itina, J. Hermann, P. Delaporte and M. Sentis, Appl. Surf. Sci. **208-209**, 27 (2003).

[19] S. I. Anisimov, D. Bäuerle and B. S. Luk'yanchuk, Phys. Rev. B. **48**, 12076 (1993).

[20] A. Kar and J. Mazumder, Phys. Rev. E. **49**, 410 (1994).

[21] A. V. Gusarov, A. G. Gnedovets and I. Smurov, J. Appl. Phys. **88**, 4352 (2000).

[22] J. C. S. Kools, T. S. Baller, S. T. De Zwart and J. Dieleman, J. Appl. Phys. **71**, 4547 (1992).

[23] J. C. S. Kools, E. van de Riet and J. Dieleman, Appl. Surf. Sci. **69**, 133 (1993).

[24] S. K. Hau, K. H. Wong, P. W. Chan and C. L. Choy, Appl. Phys. Lett. **66**, 245 (1995).

[25] J. G. Lunney, Appl. Surf. Sci. **86**, 79 (1995).

[26] R. Jordan, D. Cole, J. G. Lunney, K. Mackay and D. Givord, Appl. Surf. Sci. **86**, 24 (1995).

[27] S. Fähler, H. U. Krebs, Appl. Surf. Sci. **96-98**, 61 (1996).

[28] A. R. González-Elipe, G. Munuera and J. P. Espinos, Surf. Sci. **220**, 368 (1989).

[29] V. E. Henrich, G. Dresselhaus and H. J. Zeiger, Phys. Rev. B. **17**, 4908 (1978).

Chapter 4

Conclusion

Figure 4.1 shows schematic illustration of growth parameters we investigated here. Although, it has been recognized that each parameter has unique effect to the growth dynamics, the interactions of them have not been verified yet. The laser parameters are one of the main reasons of lack of comprehensive understanding of PLD growth. In this thesis, we examined the laser parameter effects on the growth dynamics via the properties of homoepitaxial $SrTiO_3$ films. In order to control the laser parameters such as spot size and fluence accurately, we designed a new zoom stage modeled after "quartet zoom stage". It enables us to tune the spot size systematically and obtain the high fluence over 20 J/cm^2.

We grew homoepitaxial $SrTiO_3$ films by varying laser parameters and growth temperature. We found strong influence of the laser parameters on the film properties such as c-axis lattice elongation and conductivity, which was not studied previously. EELS measurements revealed the possibility of less confinement of oxygen vacancies in film structures. These results indicated several insights of the interactions of these parameters. So long as we studied, thermal diffusion of adatoms would not be equivalent to the kinetic energies of impinging particles. Spot size is a critical factor for plume expansion which has strong influence to the films properties in cooperation with highly energetic ions in the plume. Although, detailed comparison is lacking, we claimed that the relation of these parameters can strongly modify the properties of homoepitaxial $SrTiO_3$ films. There are still several growth parameters that we have not considered yet such as the oxygen partial pressure, target-substrate distance and frequency. We hope that this study would be milestone of comprehensive understanding the growth dynamics of PLD,

which would greatly broaden the applicable field of PLD.

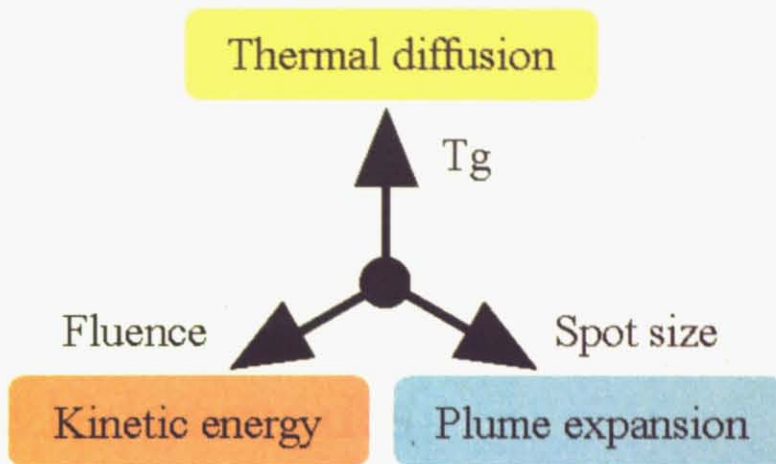

Figure 4.1: Schematic illustration of growth parameters we studied and its effect to the growth dynamics.

Chapter 5

Acknowledgements

The present work is carried out at Hwang Laboratory, in Department of Advanced Materials Science, Graduate School of Frontier Sciences, The University of Tokyo. First of all, I would like to express my gratitude from bottom of my heart to Prof. Harold Y. Hwang for his constructive advice and continuous encouragement for the progress of this study.

Also, I would like to express my deepest thanks to Dr. Tomofumi Susaki for his continuous support. He gave a lot of fruitful and helpful suggestions and discussions.

I am thankful to Dr. Tsuyoshi Ohnishi and Prof. Mikk Lippmaa for their discussion about homoepitaxial films of $SrTiO_3$. They generously opened their precious data for our progress which became a valuable guide of this study.

I appreciate Mr. Gerwin Hassink, who taught us how to design the zoom stage. Without his optics calculation, we could not construct our quartet-zoom stage. His design is a base of our zoom stage.

I appreciate Prof. David A. Muller and Ms. Lena Fitting for technical supports for TEM study.

I thank Mr. Motoshi Nakayama, who worked with me and grew a lot of samples.

Finally, I would like to express my sincere gratitude to co-workers, Dr. Naoyuki Nakagawa, Dr. Yasushi Hotta, Mr. Yasuyuki Hikita, Mr. Yusuke Tateyama, Mr. Shin Yoshida, Mr. Yusuke Kozuka, Mr. Shinsuke Nishiki, Mr. Koki Fukui and Mrs. Makiko Tanaka for having meaningful time.